Embryonic and postnatal neurogenesis produce functionally distinct subclasses of dopaminergic neuron

Elisa Galliano[1,2], Eleonora Franzoni[1], Marine Breton[1,3], Annisa N. Chand[1,4], Darren J. Byrne[1], Venkatesh N. Murthy[2] and Matthew S. Grubb[1]

1. Centre for Developmental Neurobiology, King's College London, New Hunt's House, Guy's Campus, London SE1 1UL, UK
2. Center for Brain Science and Department of Molecular and Cellular Biology, Harvard University, 16 Divinity Avenue, 02138 Cambridge MA, USA
3. Present address: Centre de Recherche en Neurosciences de Lyon Inserm U1028 - CNRS UMR5292 UCBL1, 50 Avenue Tony Garnier 69366, Lyon, France
4. Present address: Institut für Neuropathologie, Charité - Universitätsmedizin Berlin, Charitéplatz 1, 10117 Berlin, Germany

Correspondence should be addressed to Elisa Galliano (elisa.galliano@kcl.ac.uk) and Matthew Grubb (matthew.grubb@kcl.ac.uk)

Abstract

Most neurogenesis in the mammalian brain is completed embryonically, but in certain areas the production of neurons continues throughout postnatal life. The functional properties of mature postnatally-generated neurons often match those of their embryonically-produced counterparts. However, we show here that in the olfactory bulb (OB), embryonic and postnatal neurogenesis produce functionally distinct subpopulations of dopaminergic (DA) neurons. We define two subclasses of OB DA neuron by the presence or absence of a key subcellular specialisation: the axon initial segment (AIS). Large AIS-positive axon-bearing DA neurons are exclusively produced during early embryonic stages, leaving small anaxonic AIS-negative cells as the only DA subtype generated via adult neurogenesis. These populations are functionally distinct: large DA cells are more excitable, yet display weaker and – for certain long-latency or inhibitory events – more broadly-tuned responses to odorant stimuli. Embryonic and postnatal neurogenesis can therefore generate distinct neuronal subclasses, placing important constraints on the functional roles of adult-born neurons in sensory processing.

Introduction

The adult central nervous system has been long believed to be incapable of self-regeneration. Five decades ago, however, pioneering studies revealed the existence of well-defined neurogenic niches in the brain of adult rodents (Altman, 1962). Such neurogenic zones are small, spatially defined and give rise to two broad neuronal populations: hippocampal dentate granule cells, and interneurons in the olfactory bulb (OB) (Lledo et al., 2006). These newly-generated cells are believed to bring unique properties to existing networks, largely by virtue of the specialised functional and plastic features associated with their transient immature status (*e.g.*, (Carleton et al., 2003; Ge et al., 2007; Gu et al., 2012; Livneh et al., 2014; Marin-Burgin and Schinder, 2012; Nissant et al., 2009; Schmidt-Hieber et al., 2004), but see (Sailor et al., 2016)). Once fully mature, though, the functional properties of adult-generated neurons in both the hippocampus and olfactory bulb often closely match those of their developmentally-generated neighbours (*e.g.*, (Carleton et al., 2003; Grubb et al., 2008; Laplagne et al., 2006; Marin-Burgin and Schinder, 2012; Nissant et al., 2009) , but see (Valley et al., 2013)). Does this mean, then, that within broad classes of neuron – for example, dentate granule cells, or OB granule cells – embryonic and postnatal neurogenesis always produce fundamentally similar cell types?

Among the wider population of adult-generated OB cells is a heterogeneous group of inhibitory neurons situated in the structure's glomerular layer, whose main role is to modulate the earliest stages of sensory information processing (Alonso et al., 2012; Fukunaga et al., 2014; Grubb et al., 2008; Livneh et al., 2014; Livneh and Mizrahi, 2012). Different subclasses of glomerular layer interneuron can be identified by their specific expression of calcium-binding proteins (Kosaka and Kosaka, 2011), while another major subclass is identified by its ability to co-release both GABA and dopamine (Borisovska et al., 2013; Vaaga et al., 2017). These dopaminergic (DA) interneurons can be generated via adult neurogenesis (Adam and Mizrahi, 2011; Bonzano et al., 2016; De Marchis et al., 2007), and the survival of postnatally-generated DA cells is activity-dependent (Bonzano et al., 2014). Moreover, adult-born DA cells have been shown to contribute to specific olfactory behaviours (Lazarini et al., 2014).

In recent years the manner in which resident and adult-generated DA neurons contribute to olfactory processing has been widely studied, and there is now an accumulating - and sometimes contrasting - body of evidence on the role played by DA cells in glomerular circuits. A wide spectrum of functions has been proposed for these cells, involving either local or broadly-distributed actions

within the glomerular layer, and roles as diverse as modulating release from olfactory sensory neuron terminals, signal normalisation, contrast enhancement, and temporal decorrelation (Banerjee et al., 2015; Cavarretta et al., 2016; Economo et al., 2016; Liu et al., 2013; Mainland et al., 2014; Pignatelli and Belluzzi, 2017; Roland et al., 2016; Vaaga et al., 2017). The complexity and sometimes mutually exclusive nature of such functions – especially in relation to spatial connectivity – make it unlikely that a single class of interneuron could perform them all. Indeed, morphological variability has been demonstrated among OB DA neurons, and has been linked to their time of birth (Halasz et al., 1981; Kiyokage et al., 2010; Kosaka and Kosaka, 2007; Kosaka et al., 2008; Kosaka and Kosaka, 2009; Kosaka and Kosaka, 2011; Kosaka and Kosaka, 2016; McLean and Shipley, 1988; Pignatelli and Belluzzi, 2017; Pignatelli et al., 2005). However, no discrete features demarcating distinct OB DA subpopulations have yet been identified. More importantly, nothing is currently known regarding the functional properties of putative OB DA subtypes. Are there physiological differences between embryonically-generated and adult-born DA cells? And might such differences start to account for the various functional roles ascribed to this cell type in sensory processing?

Here, we build on previous work *in vitro* (Chand et al., 2015), to show that different classes of OB DA neuron *in vivo* can be clearly distinguished based on the presence or absence of an axon and its key subcellular specialisation, the axon initial segment (AIS). AIS-positive DA cells are larger, with broader dendritic arborisations, and are exclusively born in early embryonic development. Postnatally-generated DA cells, in contrast, are all small and anaxonic. Crucially, these morphological and ontological distinctions also map onto clear functional differences in both cellular excitability and odorant response properties *in vivo*, strongly constraining the potential role of adult-born DA cells in sensory processing.

Results

The axon initial segment is only present in a distinct subset of DA cells

To investigate the presence of an axon initial segment (AIS) in DA cells we performed immunohistochemistry on fixed slices of the olfactory bulb of juvenile (P28) wild-type C57Bl6 mice. We identified DA cells by labelling them with an antibody against tyrosine hydroxylase (TH), the rate-limiting enzyme in the biosynthesis of dopamine. For AIS identification we stained for ankyrin-G, the master AIS organising molecule (AnkG, Fig.1A) (Hedstrom et al., 2008; Jenkins et al., 2015; Zhou et al., 1998). While for most TH-positive cells we could not detect AnkG label on any of their processes, we identified a subset of large DA neurons that possessed a clear AnkG-positive AIS (Fig. 1A, middle and right panel; (Kosaka et al., 2008)). Like their midbrain DA (González-Cabrera et al., 2017; Meza et al., 2018) and cultured (Chand et al., 2015) counterparts, the AISs of OB DA neurons were often thin, short and located rather distally away from the soma. Along with the dense and highly interwoven meshwork of TH-positive processes in the glomerular layer (GL), this made AIS-positive cells difficult to identify. Nevertheless, a lower-bound estimate (see Methods) suggests they comprise at least 2.5 % of the overall OB DA population.

Soma size quantification revealed these AIS-containing DA neurons to be morphologically distinct. As shown in Figure 1B, the soma area distribution of the general bulbar TH+ population is clearly not unimodal (blue distribution): most DA cells are relatively small (peak 55 μm^2), but there is a distinct minority that are significantly larger (peak 140 μm^2) (Kosaka and Kosaka, 2007; McLean and Shipley, 1988; Pignatelli et al., 2005). In contrast, performing a similar analysis solely for TH+/AnkG+ cells (*i.e.* DA neurons with an AIS) produced a unimodal distribution centred on the large-cell peak of the full population curve (Fig. 1B, magenta line; peak 137 μm^2). Large AIS-positive cells therefore represent a distinct sub-population of OB DA neurons.

These large, AIS-positive DA neurons are also located in a specific sub-region of the GL. Dividing the GL into four sub-laminae (Fig. 1A; see Methods) revealed the overall TH-positive population to be concentrated in the mid-GL (Fig. 1C). AIS-positive DA neurons, however, were mostly found in the lower portions of the GL towards the external plexiform layer (EPL) border, with very little presence in the upper or mid-GL (Fig. 1C; (Liberia et al., 2012); effect of sub-lamina × cell-type in 2-way repeated-measures ANOVA, $F_{3,66} = 35.47$, $p < 0.0001$; post-hoc Sidak's test between cell types, upper-

GL, p = 0.014; mid-GL, p < 0.0001; lower-GL, p < 0.0001; EPL border, p = 0.98; n = 24 slices from N = 3 mice).

AIS-lacking DA neurons are anaxonic

The AIS is crucial for the maintenance of axo-dendritic neuronal polarity (van Beuningen et al., 2015), and is often employed as an indicator of axonal identity (*e.g.* (Watanabe et al., 2012)), so does the absence of an AIS in the majority of small DA neurons mean that these cells do not possess an axon? Addressing this question required us to be able to identify and follow *all* of a given cell's individual processes. We therefore achieved sparse label of individual OB DA neurons, either by injecting floxed GFP-encoding viruses (either AAV or RV::dio) in embryos or neonates from VGAT-^{Cre} or DAT-^{Cre} reporter lines, or by electroporating GFP-encoding plasmid DNA in wild-type neonates (see Methods). The dopaminergic phenotype of the infected neurons was confirmed by immunohistochemical label for TH. We then adopted a dual strategy for axon identification.

First – as a positive control – we confirmed that while the AnkG-positive processes of large AIS-containing DA cells co-localised with the axonal marker TRIM-46 (Fig2A) (van Beuningen et al., 2015), this axonal marker was entirely absent from the processes of small OB DA neurons (Fig. 2B; n=10, N=3, average soma area 58 μm^2). Second – as a negative control – we analysed the expression of the dendritic marker MAP-2 (Kosik and Finch, 1987; Rolls and Jegla, 2015; van Beuningen et al., 2015). DA cells with an AIS express MAP-2 in all processes, even in the proximal axon (Fig 2C). However, as reported for other cell types (Gumy et al., 2017; van Beuningen et al., 2015), this proximal axonal MAP-2 expression fades where AnkG expression begins, and MAP2 is absent from the post-AnkG portion of the axon (Fig. 2C). Conversely, AIS-negative DA neurons express MAP-2 along the entire length of all their processes (Fig. 2D; n=10, N=3, average soma area 49 μm^2). These data strongly suggest that the presence of an AIS is indicative of axonal identity in OB DA cells, and that the small TH-positive neurons that lack an AIS are truly anaxonic.

Broader dendritic branching in AIS-positive DA neurons

Sparse labelling of individual OB DA neurons also allowed us to investigate their dendritic morphology (Fig. 3A), and this again revealed clear differences between AIS-positive and AIS-negative subtypes. Small, anaxonic DA neurons had limited dendritic arborisations that ramified across a small region of the glomerular layer (Fig. 3B, C, E, F). By contrast, the dendrites of large,

133 axon-bearing DA cells were much more broadly spread (Fig. 3D, E, F). Despite considerable cell-to-
134 cell morphological variability within each sub-class (Fig. 3E, F), quantitative Sholl analysis (see
135 Methods) revealed highly significant cell-type differences on multiple dendritic parameters (Table 1;
136 Fig. 3E; effect of cell type in mixed model ANOVA analysis of Sholl distributions, $F_{1,36} = 5.30$,
137 $p = 0.027$). This is all the more striking given the thin OB slices necessary for AnkG label, and the
138 likely resulting underestimation of glomerular layer ramification by AIS-positive DA neurons.

139 ***AIS-positive DA neurons are exclusively born during early embryonic development, but anaxonic***
140 ***DA cells continue to undergo postnatal and adult neurogenesis***

141

142 Glomerular layer interneurons in the OB, including TH-positive DA neurons, belong to the highly
143 restricted group of neuronal types capable of regenerating throughout life via adult neurogenesis
144 (Betarbet et al., 1996; Bonzano et al., 2016; De Marchis et al., 2007; Winner et al., 2002). This
145 prolonged neurogenic capacity is often considered to be a universal and hallmark feature of these
146 inhibitory interneurons (*e.g.* (Liu et al., 2013)). However, data from birthdating experiments suggest
147 that – at least on the basis of soma size – OB DA neurons are not homogeneous in their time of
148 generation (Kosaka and Kosaka, 2009). This prompted us to ask whether the two morphological
149 subtypes of AIS-positive and AIS-negative OB DA neuron also differ developmentally.

150

151 To address this question we performed classic pulse-chase birthdating experiments. We injected
152 pregnant mice with the thymidine analogue bromodeoxyuridine (BrdU) at different gestational days
153 starting from embryonic day (E) 11, when the nascent olfactory bulb has begun to appear. We then
154 collected tissue from the progeny once they reached one month of age, and from the mothers
155 themselves to analyse adult-generated neurons (Fig. 4A). We also labelled neonatally-generated
156 bulbar interneurons via postnatal electroporation of GFP-encoding plasmid DNA injected into the
157 lateral ventricles at P1 (Fig. 4A). Cells were then immunostained for BrdU or GFP, along with TH and
158 – because of the histological processing necessary for BrdU detection – a more robust but as yet
159 mysterious marker of the AIS: the unidentified microtubule-associated protein labelled by the
160 'pIκBα' antibody (Buffington et al., 2012). For each injection time point we analysed all cells that
161 were both BrdU and TH positive, measuring soma area, and noting the presence or absence of an
162 AIS.

163

The results, presented in Fig. 4B-H, clearly show that with increasing birth age the soma area distributions lose their right-end tail, indicating that the large DA neurons are mostly born during early development (Kosaka and Kosaka, 2009). Interestingly, soma area in adult-born OB DA neurons (Fig. 4H) appeared small compared to overall DA population distributions at earlier ages, an effect that was not accounted for by either histological processing differences or cell maturation state, and which might indicate a potential specialization of this DA subpopulation that warrants investigation in future studies.

The developmental distinction between AIS-positive and –negative DA cells, however, was even clearer. AIS-positive DA neurons were exclusively born in embryonic development, with a clear peak in their generation at E11-12 (Fig. 4B,C,H) and only very few being produced between E13 and E18 (Fig. 4D-F,H). We did not find a single neonatal- or adult-born OB DA neuron that possessed an AIS (Fig. 4G,H).

To fully convince ourselves that adult-born DA neurons never possess an AIS, we had to rule out the possibility that these cells took longer than 1.5 months to fully mature. We therefore collected tissue from adult BrdU-injected mice after a prolonged chase period of 4 months (Fig. 5A). We found very few double-labelled BrdU+/TH+ cells (Fig. 5B; n = 15 cells from N = 2 mice), and all were AIS-negative. The absence of an AIS in adult-generated cells is therefore unlikely due to insufficient maturation time, and instead likely reflects a fundamental characteristic of this OB DA subtype.

These data strongly suggest that prolonged neurogenic capabilities are not a widespread property of bulbar DA neurons. Instead, adult neurogenesis is restricted to the axonless subpopulation, while large AIS-bearing cells are only born during early developmental stages. This finding raised two immediate questions concerning the production and longevity of AIS-positive neurons: 1) is there a preponderance of large AIS-positive DA cells in the neonate? And 2) do embryonically-generated AIS-positive neurons persist throughout life? To address the first question we collected tissue from newborn pups (P0) and quantified the soma area of TH-labelled DA neurons (Fig. 6A). We indeed found a right-shifted distribution of larger DA neurons at this early postnatal timepoint (Fig. 6B, Kolmogorov-Smirnov test D = 0.3581, $p < 0.01$; (McLean and Shipley, 1988)). We also obtained a slightly higher lower-bound estimate for the prevalence of AIS-positive DA cells at P0 (Fig. 6C; see Methods), at ~6 % of the overall TH-positive population. In addition, AIS-positive neurons at P0 already have large soma areas (mean ± SEM 98 ± 5 μm^2, n=16, N=2; Fig. 6D).

198 To address the second question concerning the longevity of AIS-positive DA neurons, we employed a
199 prolonged pulse-chase birthdating protocol. Mice were injected with BrdU at E12, then left until six
200 months of age, when we collected tissue and looked for AIS-positive DA neurons (Fig. 7A). As shown
201 in Fig. 7B, we were still able to find DA neurons born at E12 in the bulb of these fully adult mice. All
202 these neurons were large and the overwhelming majority carried an AIS. When we compared these
203 adult animals to littermates that had also been injected at E12 but perfused at P28, we found that
204 E12-born DA neurons in adult animals were larger (91 ± 4 μm^2; Fig 7C,D). Moreover, while in one-
205 month-old animals TH+/E12-BrdU+ cells were relatively abundant but only 25% of them were AIS-
206 positive, in adult mice TH+/E12-BrdU+ cells were rare but over 90% of them possessed an AIS (Fig.
207 7E). These findings strongly suggest that, of the mixed pool of DA neurons born at E12, the initially
208 abundant AIS-negative cells are turned over at some point before 6 months of age, to be substituted
209 by postnatally-born AIS-negative neurons. In contrast, embryonically-generated, large AIS-positive
210 cells can persist throughout adult life.

211 ***AIS-positive DA neurons possess distinct intrinsic functional properties***

212

213 Our morphological and developmental analyses revealed a clear distinction between - on the one
214 hand – embryonically-born, large and widely-branching DA neurons with an axon and AIS, and – on
215 the other – lifelong-generated, small and locally-ramifying anaxonic DA cells that do not have an AIS.
216 But do these marked ontological and structural differences also translate into functional
217 heterogeneity? To test this hypothesis we first performed whole-cell current-clamp
218 electrophysiological recordings on DA neurons in acute *ex vivo* OB slices.

219

220 We visualised DA neurons by crossing the dopaminergic reporter line DAT-Cre (Backman et al., 2006)
221 with a floxed tdTomato (tdT) reporter line (Madisen et al., 2010). In the resulting DAT-tdT mice the
222 majority of TH+ DA cells also expressed tdT (90 ± 4 % of all TH+ neurons were also tdT+; n=369, N=3;
223 Fig. 8A). The rare TH+ neurons that lacked tdT fluorescence tended to be large (Fig. 8B), suggesting
224 that while our genetic labelling strategy comprehensively identified small, anaxonic DA neurons, it
225 under-represented the large, AIS-positive DA subtype. Indeed, co-label for AnkG revealed that only
226 33% of TH+/AIS+ DA neurons also expressed tdT (Fig. 8B,C). However, tdT expression did not appear
227 to reveal any further subdivision amongst the large, AIS-positive DA cells, because we found no
228 difference in soma size between TH+/AIS+/tdT+ and TH+/AIS+/tdT- neurons (tdT+, mean ± SEM
229 118 ± 10 μm^2; tdT-, 126 ± 5 μm^2; Welch's corrected $t_{21.12} = 0.66$, $p = 0.52$). So, although DAT-tdT mice
230 do not comprehensively reveal all bulbar DA neurons, visually targeting tdT-positive cells for

electrophysiological recordings (Fig. 8C) still enables functional comparisons to be made between AIS-positive and –negative DA cell types.

Post-recording survival of bulbar DA cells for morphological or immunohistochemical analysis is notoriously difficult (A. Pignatelli, personal communication); this meant that we could not classify our recorded neurons as AIS-positive or -negative on the basis of AnkG staining. Instead, we relied on a functional indicator of AIS presence: non-somatic action potential (AP) initiation. In phase-plane plots of single spikes fired in response to 10 ms somatic current injection, the site of AP generation can be inferred from the shape of the initial, rising component of the spike waveform (Bean, 2007; Chand et al., 2015; Coombs et al., 1957; Jenerick, 1963; Khaliq et al., 2003; Shu et al., 2007). While a smooth, monophasic phase plane plot is indicative of AP initiation at the somatic recording site, cells that initiate spikes at a distance from the electrode location – almost always at the AIS (Bender and Trussell, 2012; Coombs et al., 1957; Foust et al., 2010; Kole et al., 2007; Palmer and Stuart, 2006) - display a distinctive biphasic, or 'double-bumped' phase plane plot waveform (Fig. 8E). We therefore divided our recorded DAT-tdT+ cells into monophasic and biphasic groups (see Methods; Fig. 8-figure supplement 1), which should be largely representative of AIS-negative and AIS-positive DA neurons, respectively. Indeed, we found that biphasic neurons were significantly larger than their monophasic counterparts (Fig. 8F; Table 2; (Chand et al., 2015)).

We also identified several differences in intrinsic excitability between monophasic and biphasic DAT-tdT cells. Biphasic neurons generated single APs in response to lower-amplitude somatic current injection, and initiated those APs more rapidly (Fig. 8F; Table 2). When induced to fire repeatedly in response to longer-lasting 500 ms somatic current injections of increasing intensity, biphasic cells displayed a linear input-output curve. Conversely, monophasic cells could not produce such a linear increase in spike number and soon reached a firing plateau (Fig. 8G). This resulted in monophasic cells having a significantly lower slope of their input-output curve, and a significantly lower maximum number of fired APs (Fig. 8H; Table 2). While these differences in intrinsic excitability are certainly consistent with reported functional characteristics of AIS-positive versus AIS-negative neurons (Chand et al., 2015; Zhou et al., 1998; Zonta et al., 2011), we cannot rule out contributions from other, non-AIS-dependent factors (Baranauskas et al., 2013; Eyal et al., 2014; Pignatelli et al., 2009). Nevertheless, and regardless of their underlying cause, these physiological differences point to significantly greater intrinsic excitability in the biphasic, presumptive AIS-possessing DA subpopulation.

Finally, we asked whether the above measures from our whole-cell recordings could be reliably used to classify DAT-tdT neurons as belonging to either the biphasic/AIS-positive or the monophasic/AIS-negative subtype. Applying principal component analysis (PCA; see Methods) to the five variables that differed significantly between mono- and biphasic DA cells generated primary and secondary component scores for each neuron that, when plotted against each other, revealed clear clustering by cell type (Fig. 8I). Furthermore, using a k-means classification approach with the same data (see Methods) we were able to assign our recorded cells to either the mono- or biphasic group with 85% accuracy. This suggests that, although there is considerable overlap in the functional properties of different subclasses of OB DA neuron, when taken together those properties reveal a significant distinction between putative AIS-positive and putative AIS-negative cell types.

Large, putative AIS$^+$ DA neurons respond more weakly yet are more broadly tuned to odour stimuli

We next asked whether the morphological and physiological differences between the two subtypes of OB DA neuron are associated with distinct sensory response properties *in vivo*. Do different types of OB DA cell respond differently to olfactory stimuli?

To address this question, we employed a conditional mouse line in which the Cre-dependent Ca^{2+} indicator GCamP6s was selectively expressed in OB DA neurons under the control of the DAT promoter (see Methods). We could then characterise the sensory response properties of these cells by monitoring changes in GCaMP fluorescence while animals were presented with a panel of eight odour stimuli (see Methods; Fig. 9A; (Kapoor et al., 2016)). Given the current lack of a reliable *in vivo* live AIS marker, we classified DA neurons in these experiments using the proxy measure of soma size – this can be readily measured in live neurons, and is consistently associated with AIS-positive or-negative identity across multiple datasets (Figs. 1, 3, 8). Our upper bound for cells classed as 'small' was 70 μm^2, taken from the mean soma size of confirmed AIS-positive DA cells (Fig. 1B, magenta distribution) minus two standard deviations (*i.e.* 136.7 – 2 x 33.2 μm^2). Under an assumption of normality, this cutoff excludes all but the smallest 2.5 % of AIS-containing neurons. Similarly, our lower bound for cells classed as 'big' was 99 μm^2, taken from the mean soma area of confirmed AIS-negative DA neurons labelled via GFP electroporation at P1 (Fig. 4H) plus two standard deviations (*i.e.* 65.6 + 2 x 16.6 μm^2). Again assuming normality, this cutoff excludes all but the biggest 2.5 % of AIS-lacking cells.

We then analysed the odorant response properties of small/putative AIS-negative (n = 594) and big/putative AIS-positive (n = 622) GCaMP+ cells imaged in 13 mice. It immediately became apparent that different forms of odour-evoked responses could occur in these neurons. In many cases a given odorant stimulus produced a relatively rapid increase in GCaMP fluorescence that then decayed back towards baseline – these responses, which we termed 'early excitatory' events, were the most prevalent form of odour-evoked signal in our DAT-GCaMP neurons (at least one early excitatory response was observed in 631/1216 = 52 % of cells). In other cases, stimuli produced an increase in GCaMP intensity that had a delayed onset and peaked late in a given recording sweep – these 'late excitatory' events were readily and objectively distinguishable from early excitatory events (see Methods; Fig. 9C,D) and were less frequent in our sample (245/1216 = 20 % of cells had at least one late excitatory response). Finally, we observed reasonably common examples of decreased GCaMP fluorescence upon odorant presentation. These 'inhibitory' events (at least one seen in 296/1216 = 24 % of cells) usually had delayed onset, and were perhaps detectable because of the characteristically high spontaneous activity levels in OB DA neurons (Chand et al., 2015; Pignatelli et al., 2005; Puopolo et al., 2005). Although both late excitatory and inhibitory response types were unusual in their long peak latencies (but see similar long-latency excitatory responses in OB DA cells in Banerjee et al., 2015, their Fig. 2B), and although they were more variable than early excitatory responses (Fig. 9E,F,G), analysis of responses to individual stimulus presentations revealed them nevertheless to be reliable odour-evoked events. Peak latencies for all response types had coefficients of variation that were significantly less than one, indicative of non-random event timing across individual stimulus repeats (Fig. 9F; early excitatory, mean ± SEM 0.28 ± 0.0063, Wilcoxon test vs 1, W = -198733, $p < 0.0001$; late excitatory 0.40 ± 0.017, W = -29773, $p < 0.0001$; inhibitory 0.38 ± 0.015, W = -42085, $p < 0.0001$). In addition, no response type was generated by spurious, one-off fluctuations in fluorescence – mean amplitudes for the two stimulus repeats that produced the *weakest* responses were still significantly greater than one standard deviation above baseline (Fig. 9G; early excitatory, mean ± SEM 5.38 ± 0.26, Wilcoxon test vs 1, W = 198036, $p < 0.0001$; late excitatory 2.29 ± 0.20, W = 17963, $p < 0.0001$; inhibitory 1.28 ± 0.060, W = 12954, $p < 0.0001$). Crucially, neither of these measures of response reliability differed between small and big DA neurons, showing that late excitatory and inhibitory events were not only reliable *per se*, but were also just as reliable in both cell types (peak time CV, late excitatory, fixed effect of cell-type in multilevel ANOVA, $F_{1,232} = 1.89$, $p = 0.17$; inhibitory, $F_{1,289} = 0.12$, $p = 0.75$; mean amplitude of 2 weakest responses, late excitatory, $F_{1,212} = 0.83$, $p = 0.36$; inhibitory, $F_{1,177} = 0.19$, $p = 0.67$). Most response types occurred in isolation, although we did see some examples of combined excitatory-inhibitory responses (at least one seen in 76/1216 = 6 % of cells). Overall, 817/1216 = 67 % of

332 imaged DAT-GCaMP+ cells displayed at least one response type evoked by at least one of the eight
333 odour stimuli we used.
334
335 All forms of odorant-evoked GCaMP response were observed in both big and small OB DA cell types.
336 There were, however, some significant differences in their relative prevalence in the two neuronal
337 populations. Paired, within-animal comparisons for the three major response types across the 13
338 mice in our sample revealed no significant differences in the proportions of small vs big DA neurons
339 that displayed at least one odorant-evoked fast excitatory (Fig. 9H; small cells, mean ± SEM 46 ± 7 %;
340 big cells 51 ± 6 %; paired t-test, $t_{12} = 1.10$, $p = 0.29$), or slow excitatory (Fig. 9H; small cells, 19 ± 3 %;
341 big cells 23 ± 3 %; paired t-test, $t_{12} = 1.15$, $p = 0.27$) response. However, we did see a significantly
342 higher proportion of inhibitory-responding neurons amongst the big cell population (Fig. 9H; small
343 cells, 16 ± 4 %; big cells 26 ± 6 %; Wilcoxon test, $W_{13} = 62$, $p = 0.012$).
344
345 To interrogate sensory stimulus selectivity further, we calculated a simple 'tuning index' (TI) for each
346 response type in each cell, from the sum of all stimuli producing a significant change in GCaMP
347 fluorescence (see Methods). Cells with higher TI values responded to more odorants in our 8-
348 stimulus panel. Although we acknowledge that this cannot represent a comprehensive description
349 of tuning across all of odour space, this measure nevertheless allowed us to detect differences in
350 response selectivity to a select group of odorant stimuli known to activate broad regions of the
351 dorsal OB (Livneh et al., 2014; Rokni et al., 2014). In line with previous observations (Banerjee et al.,
352 2015), we observed broad representations of odours in the responses of OB DA neurons (Fig 10A).
353 The mean TI value for all excitatory responses (early+late combined) was 1.99 across all neurons in
354 our sample, rising to 3.29 within the subset of neurons that displayed at least one excitatory
355 response. Overall, this broad tuning was shared by both big and small OB DA sub-populations.
356 However, we did observe significant cell-type-dependent differences in odour selectivity for
357 particular response types. Importantly, we found only very weak correlations between TI measures
358 calculated for the three major forms of odour-evoked response (early excitatory vs late excitatory,
359 Spearman $r = 0.018$, $p = 0.53$; early excitatory vs inhibitory, $r = 0.13$, $p < 0.0001$; late excitatory vs
360 inhibitory, $r = 0.030$, $p = 0.30$; $n = 1216$ in all cases), suggesting that TI values for early excitatory, late
361 excitatory and inhibitory events represent rather independent measures of tuning for distinct types
362 of response produced by glomerular layer circuitry. To compare these TI measures between cell
363 types, we needed powerful statistical tests that could leverage the large numbers of imaged neurons
364 in our dataset whilst accounting for significant across-animal variability (see Methods; Fig. 10B,C).
365 We therefore employed multilevel ANOVA analyses, where TI values from individual cells were

compared between small versus big cell populations nested in animal subjects (see Methods; (Aarts et al., 2014)). Using this approach, we found no effect of cell type on early excitatory TI values (Fig. 10B; fixed effect of cell-type in multilevel ANOVA, $F_{1,1180} = 2.04$, $p = 0.15$). For the most prevalent form of odour-evoked response, then, tuning was strikingly similar in small and big OB dopaminergic neurons. For both late excitatory and inhibitory response types, though, the effect of cell type on TI was significant (Fig. 10B; late excitatory, $F_{1,1214} = 5.58$, $p = 0.018$; inhibitory, $F_{1,1143} = 6.92$, $p = 0.009$), with big cells possessing consistently larger TI values on a mouse-by-mouse basis. When responding to odorant stimuli with late excitatory or inhibitory events, therefore, big OB DA cells are significantly more broadly tuned than their small-soma neighbours.

Could this broader tuning in big OB DA neurons be explained by larger, more readily detectable odour-evoked responses in this cell type? Actually, measures of event amplitudes revealed the opposite to be the case: big cells had significantly weaker responses to odorant stimuli, a highly significant effect that held across all response types (Fig. 10C; early excitatory, fixed effect of cell-type in multilevel ANOVA, $F_{1,626} = 6.58$, $p = 0.011$; late excitatory, $F_{1,244} = 4.50$, $p = 0.035$; inhibitory, $F_{1,295} = 32.69$, $p < 0.0001$). Despite their higher intrinsic excitability (Fig. 8), big, putative AIS+ DA neurons therefore do not display stronger responses to sensory stimuli *in vivo*. This unexpected effect may be because of fundamental differences between sensory stimulation *in vivo* versus direct electrical stimulation *in vitro*, or it may be due to cell-type differences in synaptic connectivity, or in the modulation of intrinsic properties in the intact OB. Additionally, it could be related to another feature of *in vivo* GCaMP activity: baseline fluorescence. Resting fluorescence was significantly higher in big cells (fixed effect of cell-type in multilevel ANOVA, $F_{1,658} = 12.00$, $p = 0.001$), while baseline noise was significantly lower in this cell type ($F_{1,1211} = 41.84$, $p < 0.0001$), and both measures, especially noise, correlated strongly with all response amplitude measures (baseline fluorescence vs early excitatory amplitude, Spearman $r = -0.49$, $p < 0.0001$, $n = 612$; vs late excitatory amplitude, $r = -0.44$, $p < 0.0001$, $n = 235$; vs inhibitory amplitude, $r = -0.58$, $p < 0.0001$, $n = 282$; baseline noise vs early excitatory amplitude, $r = 0.67$, $p < 0.0001$, $n = 631$; vs late excitatory amplitude, $r = 0.72$, $p < 0.0001$, $n = 245$; vs inhibitory amplitude, $r = 0.83$, $p < 0.0001$, $n = 296$). The increased buffering capacity associated with higher resting GCaMP levels (Svoboda et al., 1999) could therefore lead to dampened response amplitudes in big cells. Additionally, lower spontaneous fluctuations in resting activity could allow big OB DA neurons to significantly respond to odorant stimuli with lower amplitude events. However, these cell-type distinctions in baseline activity cannot account for the differences in response selectivity between big and small cell populations (Fig. 10B). Not only did we see identical big versus small cell selectivity for early excitatory events

when baseline differences might be expected to influence tuning across all response types, we also observed only weak and inconsistent correlations with the different TI measures for both baseline fluorescence and noise (baseline fluorescence vs early excitatory TI, Spearman $r = -0.05$, $p = 0.07$; vs late excitatory TI, $r = 0.15$, $p < 0.0001$; vs inhibitory TI, $r = 0.13$, $p < 0.0001$; $n = 1164$ in all cases; baseline noise vs early excitatory TI, $r = 0.075$, $p = 0.0085$; vs late excitatory TI, $r = -0.20$, $p < 0.0001$; vs inhibitory TI, $r = -0.17$, $p < 0.0001$; $n = 1216$ in all cases). Finally, we wondered whether the prolonged timecourse and therefore truncated response profiles of late excitatory and inhibitory responses (e.g. Fig. 9C, Fig. 10A) might have contributed to the functional differences observed for these event types between big and small OB dopaminergic cells. However, accurate estimates of decay kinetics found no cell-type differences in either response type (see Methods, Fig. 10-figure supplement 1).

Overall in terms of odorant response properties, therefore, big/putative AIS-positive and small/putative AIS-negative OB DA neurons differ significantly in: 1) the broader selectivity of big cells for specific odour-evoked response types; and 2) the higher resting fluorescence, lower baseline noise, and smaller response amplitudes of big cells. Moreover, these two major functional features appear to be largely independent of each other.

Discussion

Our results demonstrate the existence of two subtypes of OB DA neurons with distinct morphological, developmental and – crucially – functional characteristics. The majority of DA cells are small, locally-projecting, anaxonic neurons which fire low numbers of somatic action potentials; they are continuously generated and turned over throughout life, and have stronger odorant-evoked responses that for certain event types are more narrowly tuned. Conversely, a minority of DA cells are large, wide-branching and equipped with an axon and an AIS, from which they generate high frequency discharges of action potentials. These AIS-positive DA cells are born exclusively during early embryonic development and persist throughout life; their high excitability is nevertheless associated with weaker sensory-evoked responses *in vivo*, some types of which are more broadly tuned to odorant stimuli.

Cell-type identity and functional diversity in neuronal circuits

An absolutely crucial step in understanding information processing in any neuronal network is to build an accurate classification of its component parts (Zeng and Sanes, 2017). Cell-type identity – as determined by ontology, gene expression, morphology, connectivity, and/or physiology – is intimately linked to the functional role that any neuron can play in a given circuit. It is therefore no surprise that in recent attempts to model realistic network operations, a great deal of effort has been spent delineating just how many component parts those networks contain. In different regions of the mammalian brain, we now have comprehensive descriptions of cell-type diversity with regards to, for instance, gene expression (*e.g.* (Romanov et al., 2017; Tasic et al., 2016; Zeisel et al., 2015), neuronal morphology (*e.g.* (Cerminara et al., 2015; Parekh and Ascoli, 2015)), synaptic connectivity (*e.g.* (Morgan et al., 2016)), and sensory response properties (*e.g.*(Baden et al., 2016)), as well as combinatorial cellular-level identification schemes that multiplex several levels of description (*e.g.* (Fuzik et al., 2016; Markram et al., 2015; Sanes and Masland, 2015)). These studies show that broad cell-type distinctions must be supplemented by fine-scale subdivisions within different cell types in order to fully understand network function. Such classification schemes are no less vital in our understanding of information processing in olfactory bulb circuits, where a uniquely modular topographic organisation of sensory inputs, coupled with the constant remodelling associated with both peripheral and central adult neurogenesis, promises novel insight into the way the brain interprets and adapts to the outside world.

However, our current understanding of functional diversity amongst neuronal populations in the olfactory bulb is far from complete. In glomerular layer circuits –the first networks to process sensory information arriving from the periphery – there is at least broad consensus on the division of juxtaglomerular neurons into excitatory and inhibitory cell types: glutamatergic, vGlut-expressing external tufted cells are, on the whole, readily distinguished from their GABA-positive interneuron neighbours ((Hayar et al., 2004), but see (Tatti et al., 2014)). Furthermore, amongst those GABAergic interneurons are three neurochemically-distinct subpopulations, distinguishable (at least in mouse) by their non-overlapping expression of calretinin, calbindin, and tyrosine hydroxylase (Kosaka and Kosaka, 2007). However, although it has long been recognised that this latter group of TH-positive OB DA neurons are highly heterogeneous (Davis and Macrides, 1983; Halasz et al., 1981; Kosaka and Kosaka, 2007; Pignatelli et al., 2005), there has been significant disagreement as to the precise nature of cell sub-type identity within this population. There is as yet no definitive classification of OB DA neurons, even though such a scheme is vital for our understanding of sensory processing functions in glomerular circuits.

Two major differing approaches to classifying OB DA neurons are currently under dispute. In the first, morphological considerations, especially the fact that many OB DA neurons spread their processes across more than one glomerulus (but see (Bywalez et al., 2016)), were used to label *all* of these neurons as superficial 'short-axon' cells (SACs;(Kiyokage et al., 2010)). This DA SAC population was then further subdivided into 'oligoglomerular' and 'polyglomerular' subtypes based on the extent of ramification across the glomerular layer (Kiyokage et al., 2010). In contrast, the second approach argues that classic morphological descriptions of superficial SACs report a complete lack of glomerular arborisation, and that the term 'SAC' should not be used to describe *any* OB DA neurons (Kosaka and Kosaka, 2011; Kosaka and Kosaka, 2016). Instead, according to this scheme, small-soma DA neurons form a subset of true periglomerular cells (DA-PGCs), while large-soma DA cells that project long distances across the glomerular layer are termed 'inhibitory juxtaglomerular association neurons', or IJGAs (Kosaka and Kosaka, 2011; Kosaka and Kosaka, 2016).

This lack of agreement has led to some studies simply grouping all DA neurons into a single neurochemically- or genetically-defined class (*e.g.* (Banerjee et al., 2015)). We agree that the dopaminergic-GABAergic phenotype of these cells is one of their most striking characteristics, defining them as a distinct population of OB interneurons. Moreover, we found here that on many measures the sensory response characteristics of the overall bulbar dopaminergic population are rather homogeneous (Fig. 9,10). However, failing to identify important DA subclasses can produce

483 issues in the interpretation of their functional roles within OB networks. The division we observe
484 here may help to clarify matters substantially, and actually appears to fit reasonably well with both
485 of the alternative schemes already proposed. On the one hand, AIS-positive, large OB DA neurons
486 share many features with the 'polyglomerular' (Kiyokage et al., 2010) and 'IJGA' (Kosaka and Kosaka,
487 2011; Kosaka and Kosaka, 2016) classes. On the other hand, AIS-negative, small OB DA cells have
488 much in common with the 'oligoglomerular' (Kiyokage et al., 2010) and 'DA-PGC' (Kosaka and
489 Kosaka, 2011; Kosaka and Kosaka, 2016) subtypes. The AIS-negative class also shares important
490 morphological features with a population of DAT-expressing 'clasping SACs' identified by recent live
491 imaging of intracellular fills in acute OB slices (Bywalez et al., 2016), whose distinct dendritic
492 architecture and predominantly juxtaglomerular arborisations would appear to separate them from
493 classically-defined PGCs (Kosaka and Kosaka, 2016; Pinching and Powell, 1971). Most importantly,
494 while soma size and dendritic spread are continuous variables that do not permit simple sub-group
495 identification, the presence or absence of an axon is a discrete feature that should allow for cleaner
496 classification. Indeed, segregating OB DA neurons based on axonal criteria has enabled important
497 functional distinctions to be identified between subgroups (Fig. 8; (Chand et al., 2015)) that were not
498 evident from previous divisions based on continuous measures (Pignatelli and Belluzzi, 2017;
499 Pignatelli et al., 2005). Finally, in terms of nomenclature, we certainly feel that 'SAC' is a misleading
500 term for all OB DA neurons, unless it is acknowledged that in some cells the axon in question is so
501 short as to be non-existent. Perhaps a simple distinction between 'axonic' and 'anaxonic' OB DA
502 neurons will prove both clear and useful, although whether those subgroups represent forms of
503 classically-defined PGC, SAC or other cell types can remain a matter for debate.
504
505
506 ***Functional roles of axonic vs anaxonic DA neurons in sensory processing networks***
507
508 The existence of two distinct subgroups of DA neurons raises the obvious question: how might these
509 two subpopulations contribute to sensory processing? In the GL, inhibitory signalling can be either
510 intraglomerular or interglomerular in nature – acting within the circuitry of an individual glomerulus,
511 or acting between different glomeruli, respectively. Both AIS-positive and AIS-negative DA subtypes
512 possess dendritic processes that ramify within the glomerular neuropil (Fig. 3), so, assuming that the
513 release of GABA and/or dopamine occurs from these dendrites in both cell types ((Borisovska et al.,
514 2013; Kiyokage et al., 2017; Vaaga et al., 2017), but see (Liberia et al., 2012)), both subpopulations
515 have the potential to contribute to *intra*glomerular inhibition. This includes GABA and/or dopamine
516 inhibiting release probability at OSN presynaptic terminals via the activation of $GABA_B$ and D_2

517 receptors, respectively (Ennis et al., 2001; Hsia et al., 1999; Korshunov et al., 2017; McGann, 2013;
518 Vaaga et al., 2017). Local GABA release can also provide a brake on recurrent excitatory glomerular
519 networks (Gire and Schoppa, 2009; Murphy et al., 2005; Najac et al., 2011), as well as effecting auto-
520 disinhibition at high input strengths (Parsa et al., 2015). By acting at the levels of both input
521 terminals and projection neuron dendrites, intraglomerular inhibition produced by both subtypes of
522 OB DA neuron may subserve highly local gain control, potentially acting as a high-pass temporal and
523 contrast filter to facilitate the detection of strong odorant stimuli (*e.g.* (Banerjee et al., 2015;
524 Cavarretta et al., 2016; Cleland and Sethupathy, 2006; Gire and Schoppa, 2009; Korshunov et al.,
525 2017).
526
527 *Inter*glomerular inhibition, by contrast, would appear to be restricted solely to the subpopulation of
528 large, deep-lying, highly excitable AIS-positive OB DA neurons. Quite simply, only this population of
529 GABAergic GL interneurons has an axonal process that can signal sufficient distances between
530 glomerular networks (Figs 1,2,3; (Kiyokage et al., 2010; Kosaka and Kosaka, 2008). Given the
531 distribution of odorant information across glomeruli in a spatial map for odour identity (Murthy,
532 2011), such lateral inhibition between glomeruli has been predicted to enhance contrast between
533 individual stimulus representations, and therefore aid odorant identification and/or discrimination
534 (*e.g.* (Linster and Cleland, 2004; Uchida et al., 2000; Urban, 2002)). This lateral signal could be
535 distributed by AIS-positive DA neurons via well-described long-range GABAergic monosynaptic
536 connections onto external tufted cells (Banerjee et al., 2015; Liu et al., 2013; Whitesell et al., 2013).
537 In addition, the distal interglomerular projections of (AIS-positive) OB DAs can induce rebound
538 excitation via dopaminergic D1-receptor activation (Liu et al., 2013). Together with these cells'
539 slightly more broadly-tuned late excitatory and delayed inhibitory responses to odorant stimuli (Fig.
540 10), this delayed DA-mediated effect could contribute to the complex modulation of interglomerular
541 dynamics, especially in the later stages of stimulus processing.
542
543 Finally, there might also be a significant developmental component to the relative functional
544 contributions of axonic vs anaxonic OB DA neurons. Early in postnatal development, when neuronal
545 activity contributes to the refinement of both OSN terminals (Yu et al., 2004; Zou et al., 2004) and
546 projection neuron dendrites (Lin et al., 2000; Matsutani and Yamamoto, 2000) to individual
547 glomeruli, the large, interglomerular-projecting AIS-positive DA cell type is relatively more numerous
548 (Fig. 6B). Perhaps these inhibitory interneurons play a crucial role in co-ordinating odour-evoked
549 and/or spontaneous activity across the glomerular layer at these early ages, allowing distinct activity
550 patterns to drive anatomical segregation at the individual glomerulus level.

551

552 ***A distinct role for functional plasticity in postnatally-generated neurons?***

553

554 Perhaps the most remarkable difference between the two axonic and anaxonic DA subtypes is that
555 only the latter is generated throughout adult life. This observation is in agreement with a more
556 general trend of adult-born neurons in the olfactory bulb, where neither PGCs nor granule cells
557 possess an axon (Lledo et al., 2006). A recently observed small cohort of adult-born cortical neurons
558 is also anaxonic (Le Magueresse et al., 2011). In fact, with the notable exception of hippocampal
559 dentate granule cells, it appears that all CNS neurons constitutively born during adulthood are
560 anaxonic, contributing purely to local network activity by releasing neurotransmitter from their
561 dendrites. Indeed, one may speculate that it is simpler for a newly-generated neuron to insert itself
562 in a pre-existing network without having to extend and connect a far-reaching axonal process.
563 Accordingly, the large, axonic OB DA cells that do need to form such extensive connections are born
564 only during early development at the same time that other projection neurons are populating the
565 bulb (Treloar et al., 2010).

566

567 What is the evolutionary advantage for maintaining continuous neurogenesis of anaxonic local
568 interneurons? The answer to this question is highly dependent on understanding the exact role of
569 these small local neurons in olfactory processing. Immature adult-born neurons are distinguished by
570 their heightened potential for activity-dependent plasticity (Livneh and Mizrahi, 2012). We might
571 hypothesise, then, that a local intraglomerular gain control mechanism that can be readily modified
572 by experience allows for broader behavioural flexibility, and permits rapid adaptation to new
573 conditions in the external world (Lazarini et al., 2014; Livneh and Mizrahi, 2012; Rochefort et al.,
574 2002). Moreover, if adult neurogenesis can be seen as an extreme form of structural plasticity that
575 only one subtype of DA cells is capable of performing, it is probably reasonable to assume that more
576 standard and less dramatic forms of plasticity are also differentially expressed by anaxonic and
577 axonic cells. By definition, cells that do not have an AIS cannot undergo AIS plasticity, while *in vitro*
578 evidence suggests that large axonic OB DA cells are capable of regulating the length and position of
579 their AISs in an activity-dependent manner (Chand et al., 2015). But does this happen *in vivo*, and if
580 so, does it have an impact on the cell's processing of olfactory inputs? Additionally, are other forms
581 of activity-dependent plasticity in OB DA neurons (Banerjee et al., 2013; Bonzano et al., 2016;
582 Coppola, 2012; Hsia et al., 1999; Mizrahi, 2007; Wang et al., 2017) specific to individual axonic versus
583 anaxonic subclasses? Future studies will need to elucidate if other forms of neuronal plasticity can

584 be induced in both DA cell subtypes in response to perturbations in sensory experience, and if so,
585 how they impact on olfactory behaviour (Taylor et al., 2009; Tillerson et al., 2006).

Materials and methods

586 ***Animals***

587 Unless otherwise stated we used mice of either gender, and housed them under a 12-h light-dark
588 cycle in an environmentally controlled room with free access to water and food. Wild-type C57Bl6
589 mice (Charles River) were used either as experimental animals, or to back-cross each generation of
590 transgenic animals. The founders of our transgenic mouse lines – DAT-Cre (B6.SJL-*Slc6a3*$^{tm1.1(cre)Bkmn/J}$,
591 Jax stock 006660), VGAT-Cre (*Slc32a1*$^{tm2(cre)Lowl}$/J, Jax stock 016962), flex-tdTomato (B6.Cg–
592 Gt(ROSA)26Sor$^{tm9(CAG\text{-}tdTomato)Hze}$, Jax stock 007909), and flex-GCaMP6s animals (Ai96; B6;129S6-
593 *Gt(ROSA)26Sor*$^{tm96(CAG\text{-}GCaMP6s)Hze}$/J, Jax stock 024106) – were purchased from Jackson Laboratories. If
594 not stated otherwise, all experiments were performed at postnatal day (P) 28. All experiments were
595 performed under the auspices of UK Home Office personal and project licences held by the authors,
596 or were within institutional (Harvard University Institutional Animal Care and Use Committee) and
597 USA national guidelines.

598

599 ***Immunohistochemistry***

600 Mice were anesthetised with an overdose of pentobarbital and then perfused with 20 mL PBS with
601 heparin (20 units.mL^{-1}), followed by 20mL of 1% paraformaldehyde (PFA; TAAB Laboratories; in 3%
602 sucrose, 60 mM PIPES, 25 mM HEPES, 5 mM EGTA, and 1 mM $MgCl_2$). The olfactory bulbs were
603 dissected and post-fixed in 1 % PFA for 2-7 d, then embedded in 5 % agarose and sliced at 50 µm
604 using a vibratome (VT1000S, Leica). Free-floating slices were washed with PBS and incubated in 5 %
605 normal goat serum (NGS) in PBS/Triton/azide (0.25% triton, 0.02% azide) for 2 h at room
606 temperature. They were then incubated in primary antibody solution (in PBS/Triton/azide) for 2 d at
607 4°C. The primary antibodies used and their respective concentrations are indicated in Table 3.

Antigen	Raised in	Supplier	Working dilution
TH	Rabbit	Millipore	1:500
TH	Mouse	Millipore	1:500
TH	Chicken	Abcam	1:250
AnkG	mouse 2a	NeuroMab	1:500
AnkG	mouse 2b	NeuroMab	1:500
AnkG	mouse 1	NeuroMab	1:500
PIκBα	Rabbit	Cell Signaling	1:1000
TRIM-46	Rabbit	Gift from Casper Hoogenraad	1:500
MAP-2	mouse 1	Gift from Phillip Gordon-Weeks	1:500
BrdU	Rat	Serotec	1:200
GFP	Chicken	Abcam	1:2000
GFP	guinea pig	Synaptic Systems	1:500

Table 3. Details of primary antibodies

608
609 Slices were then washed three times for 5 minutes with PBS, before being incubated in secondary
610 antibody solution (species-appropriate Life Technologies Alexa Fluor-conjugated; 1:1000 in
611 PBS/Triton/azide) for 3 h at room temperature. After washing in PBS, slices were incubated in 0.2%
612 sudan black in 70% ethanol at room temperature for 3 min to minimise autofluorescence, and then
613 mounted on glass slides (Menzel-Gläser) with MOWIOL-488 (Calbiochem). Unless stated otherwise
614 all reagents were purchased from Sigma.
615
616 ***Birth-dating and sparse labelling***
617 To birth-date neurons we injected mice with a saline-based solution containing 50 mM
618 bromodeoxyuridine (BrdU, Sigma) and 17.5mM NaOH. Pregnant C57BL6 female mice received one
619 single intraperitoneal injection of this solution (0.075 ml/g) on the relevant gestational day;
620 pregnancy start date (E0) was investigated twice daily and confirmed by the presence of a vaginal
621 plug. Injected mothers and offspring were transcardially perfused on the relevant day, as detailed
622 above. To permit BrdU detection, slices were first incubated in 2 M HCl for 30min at 37°C, washed
623 thoroughly and then processed for immunohistochemistry as described above.
624
625 Sparse morphological labelling was achieved by injecting 2 µl of AAV9.EF1a.ChR2-YFP $^{lox/lox}$ virus (AV-
626 9-PV1522, Penn Vector Core, USA) in the lateral ventricle of P1-2 DAT^{Cre} or VGAT^{Cre} neonatal mice. A
627 combination of birth-dating and sparse labelling was accomplished by either electroporating 2 µl of
628 EGFP in the lateral ventricle of P1 C57BL6 mice, or by injecting floxed rv::dio-GFP$^{lox/lox}$ retrovirus
629 (Ciceri et al., 2013) in the lateral ventricle of E12 DAT^{Cre} embryos. All invasive surgery was performed
630 under isoflurane anesthesia, with Fast Green (0.3 mg/ml) co-injected to visually confirm positional
631 accuracy.
632 Injections in embryos were performed with an injector and a 30.5 ga needle through the uterine wall
633 into one of the lateral ventricles of the embryos. The uterine horns were then returned into the
634 abdominal cavity, the wall and the skin were sutured, and embryos were allowed to continue their
635 normal development.
636
637 Injections in neonates were performed in a semi-stereotaxic frame using a Hamilton syringe and a
638 borosilicate glass capillary (GC100-15, Harvard Apparatus). For electroporation, after the injection of
639 2 µl of GFP in the lateral ventricle, five 50ms-0.15 A electrical pulses were delivered at 1Hz with plate
640 electrodes (10mm diameter, Nepagene, Japan) oriented in such a way to drive the current dorso-
641 ventrally.
642

643

644 ***Fixed-tissue imaging and analysis***

645 All images were acquired with a laser scanning confocal microscope (Zeiss LSM 710) using
646 appropriate excitation and emission filters, a pinhole of 1 AU and a 40x oil immersion objective.
647 Laser power and gain were set to either prevent signal saturation in channels imaged for localisation
648 analyses, or to permit clear delineation of neuronal processes in channels imaged for neurite
649 identification (*e.g.* TH, GFP).

650

651 In *ex vivo* tissue, for branching patterns and reconstructions, images were taken with a 1x zoom
652 (0.415 µm/pixel), 512x512 pixels, and in z-stacks with 1 µm steps. For AIS identification, images were
653 taken with 3x zoom, 512x512 pixels (0.138 µm/pixel) and in z-stacks with 0.45 µm steps. All
654 quantitative analysis was performed with Fiji (Image J). AISs were identified by confirming double
655 labelling in 3D of TH along with a contiguous, elongated AnkG-positive stretch of neurite, and by
656 then following the AnkG-positive process backwards to a clearly identifiable TH-positive cell body.
657 Cell position in the glomerular layer (GL; defined by the perimeter of TH immunofluorescence) was
658 classified as: a) 'upper' if the soma bordered with both the GL and the olfactory nerve layer; b)
659 'middle' if the soma was fully embedded in the GL; c) 'lower' if the soma bordered with both the GL
660 and external plexiform layer (EPL); and d) 'EPL border' if the soma did not border at all with the GL.
661 Soma area was measured at the cell's maximum diameter, by experimenters blind to cell type
662 identity. Independent soma area measurements by two experimenters on a subset of TH-positive
663 cells revealed extremely high levels of agreement (Pearson $r = 0.97$, $n = 58$). Soma-to-OSN layer
664 distance was calculated from a straight perpendicular line connecting the cell body to the outer
665 border of TH immunofluorescence. Morphological reconstructions of neurons that were sufficiently
666 sparsely and brightly labelled were obtained with the auto-tracing Neuron 2.0 function in Vaa3D-
667 3.20. Sholl analysis was performed on traced images using the automated Image J function, with a
668 fixed first circle radius of 10 µm, and 5 µm increments for the following concentric circles. The
669 number and length of primary dendrites was manually calculated with the freehand drawing
670 function of Image J.

671

672 The density of AIS-positive DA neurons at P28 was calculated as follows. First, the average density of
673 TH-positive cells per cubic millimetre of GL was calculated by manually counting cells and measuring
674 GL area in medium magnification stacks (~43,000 cells / mm^3; 40x objective, zoom 1; n=14 slices, N=3
675 mice). Second, the total volume of tissue used to identify a total of 297 AIS- and TH-positive cells was
676 estimated by manually drawing GL area profiles in low magnification images (~0.28 mm^3; 5x

objective; n=81, N=9) and multiplying by the slice thickness (50 µm). The estimated number of TH-positive cells in this volume (~11,801) was then calculated by multiplying GL volume by the previously defined average TH-positive density per cubic millimetre. Finally, the AIS-positive/TH-positive cell percentage was calculated by dividing the total number of identified AIS-positive/TH-positive cells (297) by the estimated number of TH-positive cells present in the analysed volume. In P0 tissue, the proportion of axon-bearing DA neurons was calculated by manually counting the number of TH-positive cells in 20 stacks (n = 239, N = 2), and confirming with TRIM-46 co-label the subset of those with an axonal process (n = 14).

Acute slice electrophysiology

P21-35 DAT^{Cre}-tdTomato mice were decapitated under isoflurane anaesthesia and the OB was removed and transferred into ice-cold slicing medium containing (in mM): 240 sucrose, 5 KCl, 1.25 Na_2HPO_4, 2 $MgSO_4$, 1 $CaCl_2$, 26 $NaHCO_3$ and 10 D-Glucose, bubbled with 95%O_2 and 5% CO_2. Horizontal slices (300 µm thick) of the olfactory bulb were cut using a vibratome (VT1000S, Leica) and maintained in ACSF containing (in mM): 124 NaCl, 5 KCl, 1.25 Na_2HPO_4, 2 $MgSO_4$, 2 $CaCl_2$, 26 $NaHCO_3$ and 20 D-Glucose, bubbled with 95% O_2 and 5% CO_2 for >1 hr before experiments began.

Whole-cell patch-clamp recordings were performed using an Axopatch amplifier 700B (Molecular Devices, San Jose, CA, USA) at physiologically-relevant temperature (32-34°C) with an in-line heater (TC-344B, Warner Instruments). Signals were digitised (Digidata 1550, Molecular Devices) and Bessel-filtered at 3 kHz. Recordings were excluded if series (RS) or input (RI) resistances (assessed by -10 mV voltage steps following each test pulse, acquisition rate 20KHz) were respectively bigger than 30 MΩ or smaller than 100 MΩ, or if they varied by > 20% over the course of the experiment. Fast capacitance was compensated in the on-cell configuration and slow capacitance was compensated after rupture. Recording electrodes (GT100T-10, Harvard Apparatus) were pulled with a vertical puller (PC-10, Narishige) and filled with an intracellular solution containing (in mM): 124 K-Gluconate, 9 KCl, 10 KOH, 4 NaCl, 10 HEPES, 28.5 Sucrose, 4 Na_2ATP, 0.4 Na_3GTP (pH 7.25-7.35; 290 MOsm) and Alexa 488 (1:150). DA cells were visualised using an upright microscope (FN1, Nikon, Tokyo, Japan) equipped with a 40X water immersion objective, and tdT / Alexa 488 fluorescence was revealed by LED (CoolLED pE-100) excitation. Post-patch fill with Alexa 488 was used both to confirm tdT-positive cell identity, and to measure soma area (ImageJ) in live images captured via a SciCam camera (Scientifica).

711

712 In current-clamp mode, evoked spikes were measured with V_{hold} set to −60 ± 3 mV. For action
713 potential waveform measures, we injected 10-ms-duration current steps of increasing amplitude
714 until we reached the current threshold at which the neuron reliably fired an action potential (V_m > 0
715 mV; acquisition rate 200KHz). For multiple spiking measures, we injected 500-ms-duration current
716 steps from 0pA of increasing amplitude (Δ2pA) until the neuron passed its maximum firing frequency
717 (acquisition rate 50KHz).

718

719 Exported traces were analysed using either ClampFit (pClamp10, Molecular Devices) or custom-
720 written routines in MATLAB (Mathworks). Before differentiation for *dV*/*dt* and associated phase
721 plane plot analyses, recordings at high temporal resolution (5 µs sample interval) were smoothed
722 using a 20 point (100 µs) sliding filter. Monophasic versus biphasic phase plane plots were then
723 visually determined independently by EG and MSG. We classified completely monotonic plots with
724 continually increasing rate-of-rise as monophasic, and any plots showing a clear inflection in rate-of-
725 rise over the initial rising phase as biphasic. Any discrepancies in classification were resolved by
726 mutual agreement. We also corroborated our subjective classification using a quantitative measure
727 of spike onset sharpness: the ratio of errors produced by linear and exponential fits to the
728 perithreshold portion of the phase plane plot (Baranauskas et al., 2010; Volgushev et al., 2008). Fit
729 error ratios were calculated with a custom Matlab script written by Maxim Volgushev, using variable
730 initial portions of the phase plane plot between voltage threshold and 40 % of maximum dV/dt
731 (Baranauskas et al., 2010), for single spikes fired in response to 10 ms current injection at current
732 threshold and up to 3 subsequent suprathreshold sweeps. Using strict, established (Baranauskas et
733 al., 2010), but non-inclusive criteria for 'steep' (≈ biphasic; maximum fit error ratio > 3) versus
734 'smooth' (≈ monophasic; maximum fit error ratio < 1) spike onset, we were able to objectively
735 classify phase plane plot shape in a smaller subset of our recorded DAT-tdT+ neurons. Of 13 neurons
736 classified in this manner, only 1 was classified differently by subjective vs objective criteria.
737 Importantly, the limited subset of objectively-classified cells still displayed significant differences
738 between mono- and biphasic OB dopaminergic neurons: as in the larger, subjectively-classified
739 dataset, biphasic cells had bigger soma area, and were more excitable than their monophasic
740 counterparts (Figure 8-figure supplement 1).

741

742 For quantification of AP properties, voltage threshold was taken as the potential at which *dV*/*dt* first
743 passed 10 V/s. Onset rapidness was taken from the slope of a linear fit to the phase plane plot at
744 voltage threshold. Spike width was measured at the midpoint between voltage threshold and

745 maximum voltage. Rheobase and afterhyperpolarisation values were both measured from responses
746 to 500 ms current injection, the latter from the local voltage minimum after the first spike fired at
747 rheobase. Input-output curves were constructed by simply counting the number of spikes fired at
748 each level of injected current density.
749
750
751 ***In vivo imaging***
752
753 Thirteen DAT^{Cre}-GCaMP6s mice (either gender, age 4–10 months) were anaesthetised with a mixture
754 of ketamine (100 mg/kg) and xylazine (10 mg/kg), placed in a stereotaxic apparatus and equipped
755 with a cranial window over the olfactory bulbs using a sterile 3 mm biopsy punch (Integra Miltex). A
756 custom-built titanium head plate was secured to their skull with adhesive luting cement (C&B
757 Metabond, Parkell). A coverslip (3 mm, Warner Instruments) was placed over the cranial window
758 and tissue adhesive (3M Vetbond) was used to secure the coverslip to the bone. The mice were
759 allowed a minimum of a week to recover from surgery before the first imaging session. Prior to each
760 imaging session the mice were newly anaesthetised with a mixture of ketamine (100 mg/kg) and
761 xylazine (10 mg/kg) and secured in a custom-built microscope as described previously (Kapoor et al.,
762 2016). Mice were given a maximum of one booster injection of anaesthesia per session, and were
763 never imaged on consecutive days. GCaMP was excited and imaged via a water immersion objective
764 (20x, 0.95 NA, Olympus; sterile saline was used as the fluid for the immersion objective) at 927 nm
765 using a Ti:sapphire laser (Chameleon Ultra, Coherent) with 140 fs pulse width and 80 MHz repetition
766 rate. Image acquisition, scanning, and stimulus delivery were controlled by custom-written software
767 in LabVIEW (National Instruments). Eight odors were individually delivered via a custom-built
768 olfactometer (Kapoor et al., 2016). The odour panel included: methyl propionate (Sigma, 81988),
769 methyl butyrate (Sigma, 246093), ethyl valerate (Sigma, 290866), hexanal (Sigma, 115606), methyl
770 tiglate (Penta, 13-73400), valeraldehyde (Sigma, 110132), propyl acetate (Tokyo Chemical Industry,
771 A0044), and pentyl acetate (Sigma, 109549). All odours were diluted in diethyl phthalate solvent
772 (Sigma-Aldrich) at 2% v/v.
773
774 Single-plane images of 300 x 300 pixel fields of view were acquired at 4 Hz during odour stimulation
775 trials. Trial temporal structure consisted of: 7.5 s baseline, 3 s odour delivery, 7.5 s post-odour
776 acquisition (18 s total, with 10 s inter-trial interval). All eight odours were probed sequentially, and
777 then the entire block was repeated two more times, for a total of 24 odour trials for each field of
778 view (3 repetitions per odour). Cell soma selection was performed manually in Image J, using both

779 the timecourse and the maximum intensity projections of each odour trial, and stored in a ROI mask
780 for each field of view. Soma area and mean intensity values were then extracted for each ROI with a
781 custom-written ImageJ macro, and saved as .xls and .txt files respectively. Data were then analysed
782 with custom scripts in Matlab (Mathworks). Mean response traces were calculated across 3
783 individual stimulus presentations of each odour for each cell from background-subtracted raw
784 fluorescence values, before bleach correction was carried out by extrapolation and subtraction of a
785 single exponential function fitted to the 7.5 s pre-stimulus baseline. Mean bleach-corrected baseline
786 fluorescence over a 3 s window immediately preceding odorant presentation (f) was then used to
787 generate Δf/f traces. In some analyses comparing baseline fluorescence values across different
788 animals and imaging sessions (but not when calculating Δf/f values for all other measures), this
789 baseline F value, averaged across all stimulus presentations, was normalised by the mean value for
790 all small DA cells in a given field of view. The standard deviation of Δf/f values within the 3 s pre-
791 stimulus period, averaged across all stimulus presentations, was taken as a measure of each cell's
792 baseline noise. For each cell and each odorant we then detected the point of maximum (for
793 excitatory events) and minimum (for inhibitory events) Δf/f after stimulus onset, and took response
794 amplitude as mean Δf/f over a 3 s window centred on this peak timepoint. Responses were classed
795 as significant if this amplitude value was ≥ 3 x the baseline noise for that trace.
796
797 For analyses of response reliability (Fig. 9), background subtraction, bleach correction and Δf/f
798 calculation were carried out on individual response traces. Coefficients of variability for peak
799 latencies were then calculated as sd/mean across 3 stimulus repeats. Z-scores were calculated on a
800 repeat-by-repeat basis by dividing response amplitude (as above, mean Δf/f over a 3 s window
801 centred on the peak timepoint) by the standard deviation of Δf/f values within the 3 s pre-stimulus
802 period. We then calculated the mean of the two smallest amplitude z-scores across the 3 stimulus
803 repeats.
804
805 Excitatory responses displayed a clear bimodal distribution of peak timepoints (see Fig. 9D), so in an
806 pre-analysed subsample of our data (n = 408 cells from N = 4 mice) we used unbiased k-means
807 clustering on this parameter to set a threshold timepoint at 6 s after stimulus onset – all significant
808 excitatory responses which peaked at or before this timepoint were classed as 'early', and all
809 significant excitatory responses which peaked after this timepoint were classed as 'late'. Tuning
810 index (TI) values were calculated by summing the number of stimuli producing significant responses
811 of a given type for each cell. These values were often zero, and many cells had zero TI values for all
812 response types. These non-responding cells were included in all reported TI analyses, but results

were identical in terms of significance if analyses were restricted only to those cells that displayed at least one significant response of any type to at least one odour. Amplitude measures were calculated for each cell as the mean across all odours that produced significant responses, but cell-type effects were also consistent if this was calculated as the maximum amplitude across all significant responses instead.

To estimate response decay constants for late excitatory and inhibitory responses, we started by identifying a subset of cells whose long-latency responses returned to baseline within the timeframe of our 18 s imaging sweep (late excitatory, n = 14; inhibitory, n = 44). In these cells, we compared the decay constants produced by a single exponential fit to either the 2.5 s immediately following the response peak (= 10 timepoints at 4 Hz sample rate), or to the entire post-peak response profile. We found that fitting just the 2.5 s from the response peak produced accurate decay constant estimates – the differences between partial and full fits were small, and were not significantly different from zero for either response type (Figure 10-figure supplement 1A,B; late excitatory mean ± SEM - 3.35 ± 2.26 s, Wilcoxon test vs 0, W = -21, p = 0.50; inhibitory, -0.41 ± 0.72 s, W = 221, p = 0.17). Importantly, there was also no difference in the accuracy of this estimation in big versus small OB DA cells (late excitatory, fixed effect of cell type in multilevel ANOVA, $F_{1,9} = 0.92$, p = 0.36; inhibitory, $F_{1,41} = 1.22$, p = 0.28). We were then able to estimate decay constants in a larger subset of cells whose long-latency responses peaked at least 2.5s before the end of our imaging sweeps. This subset comprised 42 % and 44 % of all cells with late excitatory and inhibitory responses, respectively, proportions that did not differ between cell types (late excitatory, small cells, 42/105; big cells, 60/140, Fisher's exact test, p = 0.70; inhibitory, small cells 66/152, big cells 63/144, p > 0.99). We found slow decay constants of approximately 8-11 s for both late excitatory and inhibitory response types, but no difference in decay kinetics between big and small OB DA cells (Fig. 10-figure supplement 1C,D; late excitatory, fixed effect of cell type in multilevel ANOVA, $F_{1,98} = 0.32$, p = 0.57; inhibitory, $F_{1,113} = 0.078$, p = 0.78). Importantly, although making up only ~40 % of the total population of responding cells, the subsample of neurons for which we could accurately estimate decay kinetics was representative of our sample as a whole, with no significant differences observed between decay-estimated and -non-estimated cells on a wide range of measures (t-test or Mann-Whitney as appropriate within small and big cell subpopulations, Bonferroni-corrected p > 0.05 for soma area, baseline fluorescence, baseline noise, and response amplitude).

Statistical analysis

Statistical analysis was carried out using Prism (Graphpad), Matlab (Mathworks) or SPSS (IBM). Sample distributions were assessed for normality with the D'Agostino and Pearson omnibus test, and parametric or non-parametric tests carried out accordingly. α values were set to 0.05, and all comparisons were two-tailed. Principal component analysis (PCA) and k-means classification on electrophysiological data were performed (Matlab functions 'pca.m' and 'kmeans_lpo.m', respectively) on the 5 variables that differed significantly between monophasic and biphasic DAT-tdT neurons. All were normally distributed except onset rapidness, which was rendered normal by logarithmic transform. Results of the k-means analysis were validated with a 'leave-one-out' protocol, which revealed cell-type classification to be robust to the removal of any one cell from the dataset. For multilevel analyses of *in vivo* GCaMP data, distributions of baseline noise and response amplitude measures were rendered normal by logarithmic transform, and outliers – defined as any value with an absolute z-score > 3 – were removed (Aarts et al., 2014); a single outlier was removed from each dataset, representing < 0.5 % of each sample). These parameters were then analysed using linear mixed models (SPSS) with mouse as the subject variable. Tuning index data could not be rendered normal by any standard transforms, so were analysed using generalised linear mixed models with a negative binomial target distribution (accounting for > 90 % of sample variance; SPSS) and mouse as the subject variable. Dummy variable analysis revealed significant intracluster correlations in all cases, stressing the importance of nesting cell-by-cell data on individual mouse subjects (Aarts et al., 2014). Due to the non-normal nature of tuning index distributions, and the rarity of observing multiple different response types in any given single neuron, PCA was not attempted on our GCaMP data.

Author Contributions

EG, VNM and MSG designed experiments. EG, MB, ANC and DJB performed experiments. EG, EF, MB, DJB and MSG analysed data. EG, EF, VNM and MSG discussed the results. EG and MSG wrote the paper.

Acknowledgements

This work was supported by a Sir Henry Wellcome fellowship (103044) to EG, a Wellcome Trust Career Development Fellowship (088301), BBSRC grant (BB/N014650/1) and ERC Consolidator Grant (725729; FUNCOPLAN) to MSG, a Medical Research Council 4 year PhD studentship to DJB, and an NIH grant (DC013329) to VNM. We wish to thank Casper Hoogenraad and Phillip Gordon-Weeks for

antibodies, Maxim Volgushev for Matlab code, Mackenzie Mathis for DAT-GCaMP6s animals, Guilherme Neves and Lynette Lym for technical assistance with viral injections, and Vikrant Kapoor and Joseph Zak for guidance with *in vivo* imaging. Gordon Shepherd, Pierre-Marie Lledo, Oscar Marin, Juan Burrone, and all members of the Grubb and Murthy laboratories provided helpful discussions, while Alex Fleischmann and Ian Thompson made invaluable comments on the manuscript.

References

Aarts, E., M. Verhage, J.V. Veenvliet, C.V. Dolan, and S. van der Sluis. 2014. A solution to dependency: using multilevel analysis to accommodate nested data. *Nat Neurosci*. 17:491-496.

Adam, Y., and A. Mizrahi. 2011. Long-term imaging reveals dynamic changes in the neuronal composition of the glomerular layer. *J Neurosci*. 31:7967-7973.

Alonso, M., G. Lepousez, W. Sebastien, C. Bardy, M.M. Gabellec, N. Torquet, and P.M. Lledo. 2012. Activation of adult-born neurons facilitates learning and memory. *Nat Neurosci*. 15:897-904.

Altman, J. 1962. Are new neurons formed in the brains of adult mammals? *Science*. 135:1127-1128.

Backman, C.M., N. Malik, Y. Zhang, L. Shan, A. Grinberg, B.J. Hoffer, H. Westphal, and A.C. Tomac. 2006. Characterization of a mouse strain expressing Cre recombinase from the 3' untranslated region of the dopamine transporter locus. *Genesis*. 44:383-390.

Baden, T., P. Berens, K. Franke, M. Roman Roson, M. Bethge, and T. Euler. 2016. The functional diversity of retinal ganglion cells in the mouse. *Nature*. 529:345-350.

Banerjee, A., F. Marbach, F. Anselmi, M.S. Koh, M.B. Davis, P. Garcia da Silva, K. Delevich, H.K. Oyibo, P. Gupta, B. Li, and D.F. Albeanu. 2015. An Interglomerular Circuit Gates Glomerular Output and Implements Gain Control in the Mouse Olfactory Bulb. *Neuron*. 87:193-207.

Banerjee, K., Y. Akiba, H. Baker, and J.W. Cave. 2013. Epigenetic control of neurotransmitter expression in olfactory bulb interneurons. *International journal of developmental neuroscience : the official journal of the International Society for Developmental Neuroscience*. 31:415-423.

Baranauskas, G., Y. David, and I.A. Fleidervish. 2013. Spatial mismatch between the Na+ flux and spike initiation in axon initial segment. *Proc Natl Acad Sci U S A*. 110:4051-4056.

Baranauskas, G., A. Mukovskiy, F. Wolf, and M. Volgushev. 2010. The determinants of the onset dynamics of action potentials in a computational model. *Neuroscience*. 167(4):1070-1090.

Bean, B.P. 2007. The action potential in mammalian central neurons. *Nat Rev Neurosci*. 8:451-465.

Bender, K.J., and L.O. Trussell. 2012. The physiology of the axon initial segment. *Annu Rev Neurosci*. 35:249-265.

Betarbet, R., T. Zigova, R.A. Bakay, and M.B. Luskin. 1996. Dopaminergic and GABAergic interneurons of the olfactory bulb are derived from the neonatal subventricular zone. *International journal of developmental neuroscience : the official journal of the International Society for Developmental Neuroscience*. 14:921-930.

Bonzano, S., S. Bovetti, A. Fasolo, P. Peretto, and S. De Marchis. 2014. Odour enrichment increases adult-born dopaminergic neurons in the mouse olfactory bulb. *Eur J Neurosci*. 40:3450-3457.

Bonzano, S., S. Bovetti, C. Gendusa, P. Peretto, and S. De Marchis. 2016. Adult Born Olfactory Bulb Dopaminergic Interneurons: Molecular Determinants and Experience-Dependent Plasticity. *Frontiers in neuroscience*. 10:189.

Borisovska, M., A.L. Bensen, G. Chong, and G.L. Westbrook. 2013. Distinct modes of dopamine and GABA release in a dual transmitter neuron. *J Neurosci*. 33:1790-1796.

Buffington, S.A., J.M. Sobotzik, C. Schultz, and M.N. Rasband. 2012. IkappaBalpha is not required for axon initial segment assembly. *Molecular and cellular neurosciences*. 50:1-9.

Bywalez, W.G., T. Ona-Jodar, M. Lukas, J. Ninkovic, and V. Egger. 2016. Dendritic Arborization Patterns of Small Juxtaglomerular Cell Subtypes within the Rodent Olfactory Bulb. *Frontiers in neuroanatomy*. 10:127.

Carleton, A., L.T. Petreanu, R. Lansford, A. Alvarez-Buylla, and P.M. Lledo. 2003. Becoming a new neuron in the adult olfactory bulb. *Nat Neurosci*. 6:507-518.

Cavarretta, F., A. Marasco, M.L. Hines, G.M. Shepherd, and M. Migliore. 2016. Glomerular and Mitral-Granule Cell Microcircuits Coordinate Temporal and Spatial Information Processing in the Olfactory Bulb. *Frontiers in computational neuroscience*. 10:67.

Cerminara, N.L., E.J. Lang, R.V. Sillitoe, and R. Apps. 2015. Redefining the cerebellar cortex as an assembly of non-uniform Purkinje cell microcircuits. *Nat Rev Neurosci*. 16:79-93.

Chand, A.N., E. Galliano, R.A. Chesters, and M.S. Grubb. 2015. A distinct subtype of dopaminergic interneuron displays inverted structural plasticity at the axon initial segment. *J Neurosci*. 35:1573-1590.

Ciceri, G., N. Dehorter, I. Sols, Z.J. Huang, M. Maravall, and O. Marin. 2013. Lineage-specific laminar organization of cortical GABAergic interneurons. *Nat Neurosci*. 16:1199-1210.

Cleland, T.A., and P. Sethupathy. 2006. Non-topographical contrast enhancement in the olfactory bulb. *BMC neuroscience*. 7:7.

Coombs, J.S., D.R. Curtis, and J.C. Eccles. 1957. The generation of impulses in motoneurones. *J Physiol*. 139:232-249.

Coppola, D.M. 2012. Studies of olfactory system neural plasticity: the contribution of the unilateral naris occlusion technique. *Neural plasticity*. 2012:351752.

Davis, B.J., and F. Macrides. 1983. Tyrosine hydroxylase immunoreactive neurons and fibers in the olfactory system of the hamster. *The Journal of Comparative Neurology*:27-440.

De Marchis, S., S. Bovetti, B. Carletti, Y.C. Hsieh, D. Garzotto, P. Peretto, A. Fasolo, A.C. Puche, and F. Rossi. 2007. Generation of distinct types of periglomerular olfactory bulb interneurons during development and in adult mice: implication for intrinsic properties of the subventricular zone progenitor population. *J Neurosci*. 27:657-664.

Economo, M.N., K.R. Hansen, and M. Wachowiak. 2016. Control of Mitral/Tufted Cell Output by Selective Inhibition among Olfactory Bulb Glomeruli. *Neuron*. 91:397-411.

Ennis, M., F.M. Zhou, K.J. Ciombor, V. Aroniadou-Anderjaska, A. Hayar, E. Borrelli, L.A. Zimmer, F. Margolis, and M.T. Shipley. 2001. Dopamine D2 receptor-mediated presynaptic inhibition of olfactory nerve terminals. *J Neurophysiol*. 86:2986-2997.

Eyal, G., H.D. Mansvelder, C.P. de Kock, and I. Segev. 2014. Dendrites impact the encoding capabilities of the axon. *J Neurosci*. 34:8063-8071.

Foust, A., M. Popovic, D. Zecevic, and D.A. McCormick. 2010. Action potentials initiate in the axon initial segment and propagate through axon collaterals reliably in cerebellar Purkinje neurons. *J Neurosci*. 30:6891-6902.

Fukunaga, I., J.T. Herb, M. Kollo, E.S. Boyden, and A.T. Schaefer. 2014. Independent control of gamma and theta activity by distinct interneuron networks in the olfactory bulb. *Nat Neurosci*. 17:1208-1216.

Fuzik, J., A. Zeisel, Z. Mate, D. Calvigioni, Y. Yanagawa, G. Szabo, S. Linnarsson, and T. Harkany. 2016. Integration of electrophysiological recordings with single-cell RNA-seq data identifies neuronal subtypes. *Nature biotechnology*. 34:175-183.

Ge, S., D.A. Pradhan, G.L. Ming, and H. Song. 2007. GABA sets the tempo for activity-dependent adult neurogenesis. *Trends Neurosci*. 30:1-8.

Gire, D.H., and N.E. Schoppa. 2009. Control of on/off glomerular signaling by a local GABAergic microcircuit in the olfactory bulb. *J Neurosci*. 29:13454-13464.

González-Cabrera, C., R. Meza, L. Ulloa, P. Merino-Sepúlveda, V. Luco, A. Sanhueza, A. Oñate-Ponce, J.P. Bolam, and P. Henny. 2017. Characterization of the axon initial segment of mice substantia nigra dopaminergic neurons. *J Comp Neurol.* . 525(16):3529-3542.

Grubb, M.S., A. Nissant, K. Murray, and P.M. Lledo. 2008. Functional maturation of the first synapse in olfaction: development and adult neurogenesis. *J Neurosci*. 28:2919-2932.

Gu, Y., M. Arruda-Carvalho, J. Wang, S.R. Janoschka, S.A. Josselyn, P.W. Frankland, and S. Ge. 2012. Optical controlling reveals time-dependent roles for adult-born dentate granule cells. *Nat Neurosci*. 15:1700-1706.

Gumy, L.F., E.A. Katrukha, I. Grigoriev, D. Jaarsma, L.C. Kapitein, A. Akhmanova, and C.C. Hoogenraad. 2017. MAP2 Defines a Pre-axonal Filtering Zone to Regulate KIF1- versus KIF5-Dependent Cargo Transport in Sensory Neurons. *Neuron*. 94(2):347-362.

Halasz, N., O. Johansson, T. Hokfelt, A. Ljungdahl, and M. Goldstein. 1981. Immunohistochemical identification of two types of dopamine neuron in the rat olfactory bulb as seen by serial sectioning. *Journal of neurocytology*. 10:251-259.

Hayar, A., S. Karnup, M. Ennis, and M.T. Shipley. 2004. External tufted cells: a major excitatory element that coordinates glomerular activity. *J Neurosci*. 24:6676-6685.

Hedstrom, K.L., Y. Ogawa, and M.N. Rasband. 2008. AnkyrinG is required for maintenance of the axon initial segment and neuronal polarity. *J Cell Biol*. 183:635-640.

Hsia, A.Y., J.D. Vincent, and P.M. Lledo. 1999. Dopamine depresses synaptic inputs into the olfactory bulb. *J Neurophysiol*. 82:1082-1085.

Jenerick, H. 1963. Phase Plane Trajectories of the Muscle Spike Potential. *Biophysical journal*. 3:363-377.

Jenkins, P.M., N. Kim, S.L. Jones, W.C. Tseng, T.M. Svitkina, H.H. Yin, and V. Bennett. 2015. Giant ankyrin-G: a critical innovation in vertebrate evolution of fast and integrated neuronal signaling. *Proc Natl Acad Sci U S A*. 112:957-964.

Kapoor, V., A.C. Provost, P. Agarwal, and V.N. Murthy. 2016. Activation of raphe nuclei triggers rapid and distinct effects on parallel olfactory bulb output channels. *Nat Neurosci*. 19:271-282.

Khaliq, Z.M., N.W. Gouwens, and I.M. Raman. 2003. The contribution of resurgent sodium current to high-frequency firing in Purkinje neurons: an experimental and modeling study. *J Neurosci*. 23:4899-4912.

Kiyokage, E., K. Kobayashi, and K. Toida. 2017. Spatial distribution of synapses on tyrosine hydroxylase-expressing juxtaglomerular cells in the mouse olfactory glomerulus. *J Comp Neurol*. 525:1059-1074.

Kiyokage, E., Y.Z. Pan, Z. Shao, K. Kobayashi, G. Szabo, Y. Yanagawa, K. Obata, H. Okano, K. Toida, A.C. Puche, and M.T. Shipley. 2010. Molecular identity of periglomerular and short axon cells. *J Neurosci*. 30:1185-1196.

Kole, M.H., J.J. Letzkus, and G.J. Stuart. 2007. Axon initial segment Kv1 channels control axonal action potential waveform and synaptic efficacy. *Neuron*. 55:633-647.

Korshunov, K.S., L.J. Blakemore, and P.Q. Trombley. 2017. Dopamine: A Modulator of Circadian Rhythms in the Central Nervous System. *Front Cell Neurosci*. 11:91.

Kosaka, K., and T. Kosaka. 2007. Chemical properties of type 1 and type 2 periglomerular cells in the mouse olfactory bulb are different from those in the rat olfactory bulb. *Brain Res*. 1167:42-55.

Kosaka, T., M. Komada, and K. Kosaka. 2008. Sodium channel cluster, βIV-spectrin and ankyrinG positive “hot spots” on dendritic segments of parvalbumin-containing neurons and some other neurons in the mouse and rat main olfactory bulbs. *Neuroscience Research*. 62:176-186.

Kosaka, T., and K. Kosaka. 2008. Tyrosine hydroxylase-positive GABAergic juxtaglomerular neurons are the main source of the interglomerular connections in the mouse main olfactory bulb. *Neurosci Res*. 60:349-354.

Kosaka, T., and K. Kosaka. 2009. Two types of tyrosine hydroxylase positive GABAergic juxtaglomerular neurons in the mouse main olfactory bulb are different in their time of origin. *Neurosci Res*. 64:436-441.

Kosaka, T., and K. Kosaka. 2011. "Interneurons" in the olfactory bulb revisited. *Neurosci Res*. 69:93-99.

Kosaka, T., and K. Kosaka. 2016. Neuronal organization of the main olfactory bulb revisited. *Anatomical science international*. 91:115-127.

Kosik, K.S., and E.A. Finch. 1987. MAP2 and tau segregate into dendritic and axonal domains after the elaboration of morphologically distinct neurites: an immunocytochemical study of cultured rat cerebrum. *J Neurosci*. 7:3142-3153.

1016 Laplagne, D.A., M.S. Esposito, V.C. Piatti, N.A. Morgenstern, C. Zhao, H. van Praag, F.H. Gage, and
1017 A.F. Schinder. 2006. Functional convergence of neurons generated in the developing and
1018 adult hippocampus. *PLoS biology*. 4:e409.
1019 Lazarini, F., M.M. Gabellec, C. Moigneu, F. de Chaumont, J.C. Olivo-Marin, and P.M. Lledo. 2014.
1020 Adult neurogenesis restores dopaminergic neuronal loss in the olfactory bulb. *J Neurosci*.
1021 34:14430-14442.
1022 Le Magueresse, C., J. Alfonso, K. Khodosevich, A.A. Arroyo Martin, C. Bark, and H. Monyer. 2011.
1023 "Small axonless neurons": postnatally generated neocortical interneurons with delayed
1024 functional maturation. *J Neurosci*. 31:16731-16747.
1025 Liberia, T., J.M. Blasco-Ibanez, J. Nacher, E. Varea, V. Zwafink, and C. Crespo. 2012. Characterization
1026 of a population of tyrosine hydroxylase-containing interneurons in the external plexiform
1027 layer of the rat olfactory bulb. *Neuroscience*. 217:140-153.
1028 Lin, D.M., F. Wang, G. Lowe, G.H. Gold, R. Axel, J. Ngai, and L. Brunet. 2000. Formation of precise
1029 connections in the olfactory bulb occurs in the absence of odorant-evoked neuronal activity.
1030 *Neuron*. 26:69-80.
1031 Linster, C., and T.A. Cleland. 2004. Configurational and elemental odor mixture perception can arise
1032 from local inhibition. *J Comput Neurosci*. 16:39-47.
1033 Liu, S., C. Plachez, Z. Shao, A. Puche, and M.T. Shipley. 2013. Olfactory bulb short axon cell release of
1034 GABA and dopamine produces a temporally biphasic inhibition-excitation response in
1035 external tufted cells. *J Neurosci*. 33:2916-2926.
1036 Livneh, Y., Y. Adam, and A. Mizrahi. 2014. Odor processing by adult-born neurons. *Neuron*. 81:1097-
1037 1110.
1038 Livneh, Y., and A. Mizrahi. 2012. Experience-dependent plasticity of mature adult-born neurons. *Nat*
1039 *Neurosci*. 15:26-28.
1040 Lledo, P.M., M. Alonso, and M.S. Grubb. 2006. Adult neurogenesis and functional plasticity in
1041 neuronal circuits. *Nat Rev Neurosci*. 7:179-193.
1042 Madisen, L., T.A. Zwingman, S.M. Sunkin, S.W. Oh, H.A. Zariwala, H. Gu, L.L. Ng, R.D. Palmiter, M.J.
1043 Hawrylycz, A.R. Jones, E.S. Lein, and H. Zeng. 2010. A robust and high-throughput Cre
1044 reporting and characterization system for the whole mouse brain. *Nat Neurosci*. 13:133-140.
1045 Mainland, J.D., J.N. Lundstrom, J. Reisert, and G. Lowe. 2014. From molecule to mind: an integrative
1046 perspective on odor intensity. *Trends Neurosci*. 37:443-454.
1047 Marin-Burgin, A., and A.F. Schinder. 2012. Requirement of adult-born neurons for hippocampus-
1048 dependent learning. *Behavioural brain research*. 227:391-399.
1049 Markram, H., E. Muller, S. Ramaswamy, M.W. Reimann, M. Abdellah, C.A. Sanchez, A. Ailamaki, L.
1050 Alonso-Nanclares, N. Antille, S. Arsever, G.A. Kahou, T.K. Berger, A. Bilgili, N. Buncic, A.
1051 Chalimourda, G. Chindemi, J.D. Courcol, F. Delalondre, V. Delattre, S. Druckmann, R.
1052 Dumusc, J. Dynes, S. Eilemann, E. Gal, M.E. Gevaert, J.P. Ghobril, A. Gidon, J.W. Graham, A.
1053 Gupta, V. Haenel, E. Hay, T. Heinis, J.B. Hernando, M. Hines, L. Kanari, D. Keller, J. Kenyon, G.
1054 Khazen, Y. Kim, J.G. King, Z. Kisvarday, P. Kumbhar, S. Lasserre, J.V. Le Be, B.R. Magalhaes, A.
1055 Merchan-Perez, J. Meystre, B.R. Morrice, J. Muller, A. Munoz-Cespedes, S. Muralidhar, K.
1056 Muthurasa, D. Nachbaur, T.H. Newton, M. Nolte, A. Ovcharenko, J. Palacios, L. Pastor, R.
1057 Perin, R. Ranjan, I. Riachi, J.R. Rodriguez, J.L. Riquelme, C. Rossert, K. Sfyrakis, Y. Shi, J.C.
1058 Shillcock, G. Silberberg, R. Silva, F. Tauheed, M. Telefont, M. Toledo-Rodriguez, T. Trankler,
1059 W. Van Geit, J.V. Diaz, R. Walker, Y. Wang, S.M. Zaninetta, J. DeFelipe, S.L. Hill, I. Segev, and
1060 F. Schurmann. 2015. Reconstruction and Simulation of Neocortical Microcircuitry. *Cell*.
1061 163:456-492.
1062 Matsutani, S., and N. Yamamoto. 2000. Differentiation of mitral cell dendrites in the developing
1063 main olfactory bulbs of normal and naris-occluded rats. *J Comp Neurol*. 418:402-410.
1064 McGann, J.P. 2013. Presynaptic inhibition of olfactory sensory neurons: new mechanisms and
1065 potential functions. *Chemical senses*. 38:459-474.

McLean, J.H., and M.T. Shipley. 1988. Postmitotic, postmigrational expression of tyrosine hydroxylase in olfactory bulb dopaminergic neurons. *J Neurosci*. 8:3658-3669.
Meza, R., L. López-Jury, C.C. Canavier, and P. Henny. 2018. Role of the Axon Initial Segment in the Control of Spontaneous Frequency of Nigral Dopaminergic Neurons In Vivo. *J Neurosci*. 38(3):733-744.
Mizrahi, A. 2007. Dendritic development and plasticity of adult-born neurons in the mouse olfactory bulb. *Nat Neurosci*. 10:444-452.
Morgan, J.L., D.R. Berger, A.W. Wetzel, and J.W. Lichtman. 2016. The Fuzzy Logic of Network Connectivity in Mouse Visual Thalamus. *Cell*. 165:192-206.
Murphy, G.J., D.P. Darcy, and J.S. Isaacson. 2005. Intraglomerular inhibition: signaling mechanisms of an olfactory microcircuit. *Nat Neurosci*. 8:354-364.
Murthy, V.N. 2011. Olfactory maps in the brain. *Annu Rev Neurosci*. 34:233-258.
Najac, M., D. De Saint Jan, L. Reguero, P. Grandes, and S. Charpak. 2011. Monosynaptic and polysynaptic feed-forward inputs to mitral cells from olfactory sensory neurons. *J Neurosci*. 31:8722-8729.
Nissant, A., C. Bardy, H. Katagiri, K. Murray, and P.M. Lledo. 2009. Adult neurogenesis promotes synaptic plasticity in the olfactory bulb. *Nat Neurosci*. 12:728-730.
Palmer, L.M., and G.J. Stuart. 2006. Site of action potential initiation in layer 5 pyramidal neurons. *J Neurosci*. 26:1854-1863.
Parekh, R., and G.A. Ascoli. 2015. Quantitative investigations of axonal and dendritic arbors: development, structure, function, and pathology. *The Neuroscientist : a review journal bringing neurobiology, neurology and psychiatry*. 21:241-254.
Parsa, P.V., R.D. D'Souza, and S. Vijayaraghavan. 2015. Signaling between periglomerular cells reveals a bimodal role for GABA in modulating glomerular microcircuitry in the olfactory bulb. *Proc Natl Acad Sci U S A*. 112:9478-9483.
Pignatelli, A., J.B. Ackman, D. Vigetti, A.P. Beltrami, S. Zucchini, and O. Belluzzi. 2009. A potential reservoir of immature dopaminergic replacement neurons in the adult mammalian olfactory bulb. *Pflugers Arch*. 457:899-915.
Pignatelli, A., and O. Belluzzi. 2017. Dopaminergic Neurones in the Main Olfactory Bulb: An Overview from an Electrophysiological Perspective. *Frontiers in neuroanatomy*. 11:7.
Pignatelli, A., K. Kobayashi, H. Okano, and O. Belluzzi. 2005. Functional properties of dopaminergic neurones in the mouse olfactory bulb. *J Physiol*. 564:501-514.
Pinching, A.J., and T.P. Powell. 1971. The neuropil of the periglomerular region of the olfactory bulb. *Journal of cell science*. 9:379-409.
Puopolo, M., B.P. Bean, and E. Raviola. 2005. Spontaneous activity of isolated dopaminergic periglomerular cells of the main olfactory bulb. *J Neurophysiol*. 94:3618-3627.
Rochefort, C., G. Gheusi, J.D. Vincent, and P.M. Lledo. 2002. Enriched odor exposure increases the number of newborn neurons in the adult olfactory bulb and improves odor memory. *J Neurosci*. 22:2679-2689.
Rokni, D., V. Hemmelder, V. Kapoor, and V.N. Murthy. 2014. An olfactory cocktail party: figure-ground segregation of odorants in rodents. *Nat Neurosci*. 17:1225-1232.
Roland, B., R. Jordan, D.L. Sosulski, A. Diodato, I. Fukunaga, I. Wickersham, K.M. Franks, A.T. Schaefer, and A. Fleischmann. 2016. Massive normalization of olfactory bulb output in mice with a 'monoclonal nose'. *eLife*. 5.
Rolls, M.M., and T.J. Jegla. 2015. Neuronal polarity: an evolutionary perspective. *The Journal of experimental biology*. 218:572-580.
Romanov, R.A., A. Zeisel, J. Bakker, F. Girach, A. Hellysaz, R. Tomer, A. Alpar, J. Mulder, F. Clotman, E. Keimpema, B. Hsueh, A.K. Crow, H. Martens, C. Schwindling, D. Calvigioni, J.S. Bains, Z. Mate, G. Szabo, Y. Yanagawa, M.D. Zhang, A. Rendeiro, M. Farlik, M. Uhlen, P. Wulff, C. Bock, C. Broberger, K. Deisseroth, T. Hokfelt, S. Linnarsson, T.L. Horvath, and T. Harkany. 2017.

Molecular interrogation of hypothalamic organization reveals distinct dopamine neuronal subtypes. *Nat Neurosci*. 20:176-188.

Sailor, K.A., M.T. Valley, M.T. Wiechert, H. Riecke, G.J. Sun, W. Adams, J.C. Dennis, S. Sharafi, G.L. Ming, H. Song, and P.M. Lledo. 2016. Persistent Structural Plasticity Optimizes Sensory Information Processing in the Olfactory Bulb. *Neuron*. 91:384-396.

Sanes, J.R., and R.H. Masland. 2015. The types of retinal ganglion cells: current status and implications for neuronal classification. *Annu Rev Neurosci*. 38:221-246.

Schmidt-Hieber, C., P. Jonas, and J. Bischofberger. 2004. Enhanced synaptic plasticity in newly generated granule cells of the adult hippocampus. *Nature*. 429:184-187.

Shu, Y., A. Duque, Y. Yu, B. Haider, and D.A. McCormick. 2007. Properties of action-potential initiation in neocortical pyramidal cells: evidence from whole cell axon recordings. *J Neurophysiol*. 97:746-760.

Svoboda, K., F. Helmchen, W. Denk, and D.W. Tank. 1999. Spread of dendritic excitation in layer 2/3 pyramidal neurons in rat barrel cortex in vivo. *Nat Neurosci*. 2:65-73.

Tasic, B., V. Menon, T.N. Nguyen, T.K. Kim, T. Jarsky, Z. Yao, B. Levi, L.T. Gray, S.A. Sorensen, T. Dolbeare, D. Bertagnolli, J. Goldy, N. Shapovalova, S. Parry, C. Lee, K. Smith, A. Bernard, L. Madisen, S.M. Sunkin, M. Hawrylycz, C. Koch, and H. Zeng. 2016. Adult mouse cortical cell taxonomy revealed by single cell transcriptomics. *Nat Neurosci*. 19:335-346.

Tatti, R., K. Bhaukaurally, O. Gschwend, R.P. Seal, R.H. Edwards, I. Rodriguez, and A. Carleton. 2014. A population of glomerular glutamatergic neurons controls sensory information transfer in the mouse olfactory bulb. *Nature communications*. 5:3791.

Taylor, T.N., W.M. Caudle, K.R. Shepherd, A. Noorian, C.R. Jackson, P.M. Iuvone, D. Weinshenker, J.G. Greene, and G.W. Miller. 2009. Nonmotor symptoms of Parkinson's disease revealed in an animal model with reduced monoamine storage capacity. *J Neurosci*. 29:8103-8113.

Tillerson, J.L., W.M. Caudle, J.M. Parent, C. Gong, T. Schallert, and G.W. Miller. 2006. Olfactory discrimination deficits in mice lacking the dopamine transporter or the D2 dopamine receptor. *Behavioural brain research*. 172:97-105.

Treloar, H.B., A.M. Miller, A. Ray, and C.A. Greer. 2010. Development of the Olfactory System. *In* The Neurobiology of Olfaction. A. Menini, editor, Boca Raton (FL).

Uchida, N., Y.K. Takahashi, M. Tanifuji, and K. Mori. 2000. Odor maps in the mammalian olfactory bulb: domain organization and odorant structural features. *Nat Neurosci*. 3:1035-1043.

Urban, N.N. 2002. Lateral inhibition in the olfactory bulb and in olfaction. *Physiology & behavior*. 77:607-612.

Vaaga, C.E., J.T. Yorgason, J.T. Williams, and G.L. Westbrook. 2017. Presynaptic gain control by endogenous cotransmission of dopamine and GABA in the olfactory bulb. *J Neurophysiol*. 117:1163-1170.

Valley, M.T., L.G. Henderson, S.A. Inverso, and P.M. Lledo. 2013. Adult neurogenesis produces neurons with unique GABAergic synapses in the olfactory bulb. *J Neurosci*. 33:14660-14665.

van Beuningen, S.F., L. Will, M. Harterink, A. Chazeau, E.Y. van Battum, C.P. Frias, M.A. Franker, E.A. Katrukha, R. Stucchi, K. Vocking, A.T. Antunes, L. Slenders, S. Doulkeridou, P. Sillevis Smitt, A.F. Altelaar, J.A. Post, A. Akhmanova, R.J. Pasterkamp, L.C. Kapitein, E. de Graaff, and C.C. Hoogenraad. 2015. TRIM46 Controls Neuronal Polarity and Axon Specification by Driving the Formation of Parallel Microtubule Arrays. *Neuron*. 88:1208-1226.

Volgushev, M., A. Malyshev, P. Balaban, M. Chistiakova, S. Volgushev, and F. Wolf. 2008. Onset dynamics of action potentials in rat neocortical neurons and identified snail neurons: quantification of the difference. *PLoS One*. 3(4):e1962.

Wang, M., E. Cai, N. Fujiwara, L. Fones, E. Brown, Y. Yanagawa, and J.W. Cave. 2017. Odorant Sensory Input Modulates DNA Secondary Structure Formation and Heterogeneous Ribonucleoprotein Recruitment on the Tyrosine Hydroxylase and Glutamic Acid Decarboxylase 1 Promoters in the Olfactory Bulb. *J Neurosci*. 37:4778-4789.

Watanabe, K., S. Al-Bassam, Y. Miyazaki, T.J. Wandless, P. Webster, and D.B. Arnold. 2012. Networks of polarized actin filaments in the axon initial segment provide a mechanism for sorting axonal and dendritic proteins. *Cell Rep*. 2:1546-1553.

Whitesell, J.D., K.A. Sorensen, B.C. Jarvie, S.T. Hentges, and N.E. Schoppa. 2013. Interglomerular lateral inhibition targeted on external tufted cells in the olfactory bulb. *J Neurosci*. 33:1552-1563.

Winner, B., C.M. Cooper-Kuhn, R. Aigner, J. Winkler, and H.G. Kuhn. 2002. Long-term survival and cell death of newly generated neurons in the adult rat olfactory bulb. *Eur J Neurosci*. 16:1681-1689.

Yu, C.R., J. Power, G. Barnea, S. O'Donnell, H.E. Brown, J. Osborne, R. Axel, and J.A. Gogos. 2004. Spontaneous neural activity is required for the establishment and maintenance of the olfactory sensory map. *Neuron*. 42:553-566.

Zeisel, A., A.B. Munoz-Manchado, S. Codeluppi, P. Lonnerberg, G. La Manno, A. Jureus, S. Marques, H. Munguba, L. He, C. Betsholtz, C. Rolny, G. Castelo-Branco, J. Hjerling-Leffler, and S. Linnarsson. 2015. Brain structure. Cell types in the mouse cortex and hippocampus revealed by single-cell RNA-seq. *Science*. 347:1138-1142.

Zeng, H., and J.R. Sanes. 2017. Neuronal cell-type classification: challenges, opportunities and the path forward. *Nat Rev Neurosci*. 18:530-546.

Zhou, D., S. Lambert, P.L. Malen, S. Carpenter, L.M. Boland, and V. Bennett. 1998. AnkyrinG is required for clustering of voltage-gated Na channels at axon initial segments and for normal action potential firing. *J Cell Biol*. 143:1295-1304.

Zonta, B., A. Desmazieres, A. Rinaldi, S. Tait, D.L. Sherman, M.F. Nolan, and P.J. Brophy. 2011. A critical role for Neurofascin in regulating action potential initiation through maintenance of the axon initial segment. *Neuron*. 69:945-956.

Zou, D.J., P. Feinstein, A.L. Rivers, G.A. Mathews, A. Kim, C.A. Greer, P. Mombaerts, and S. Firestein. 2004. Postnatal refinement of peripheral olfactory projections. *Science*. 304:1976-1979.

Figures and Legends

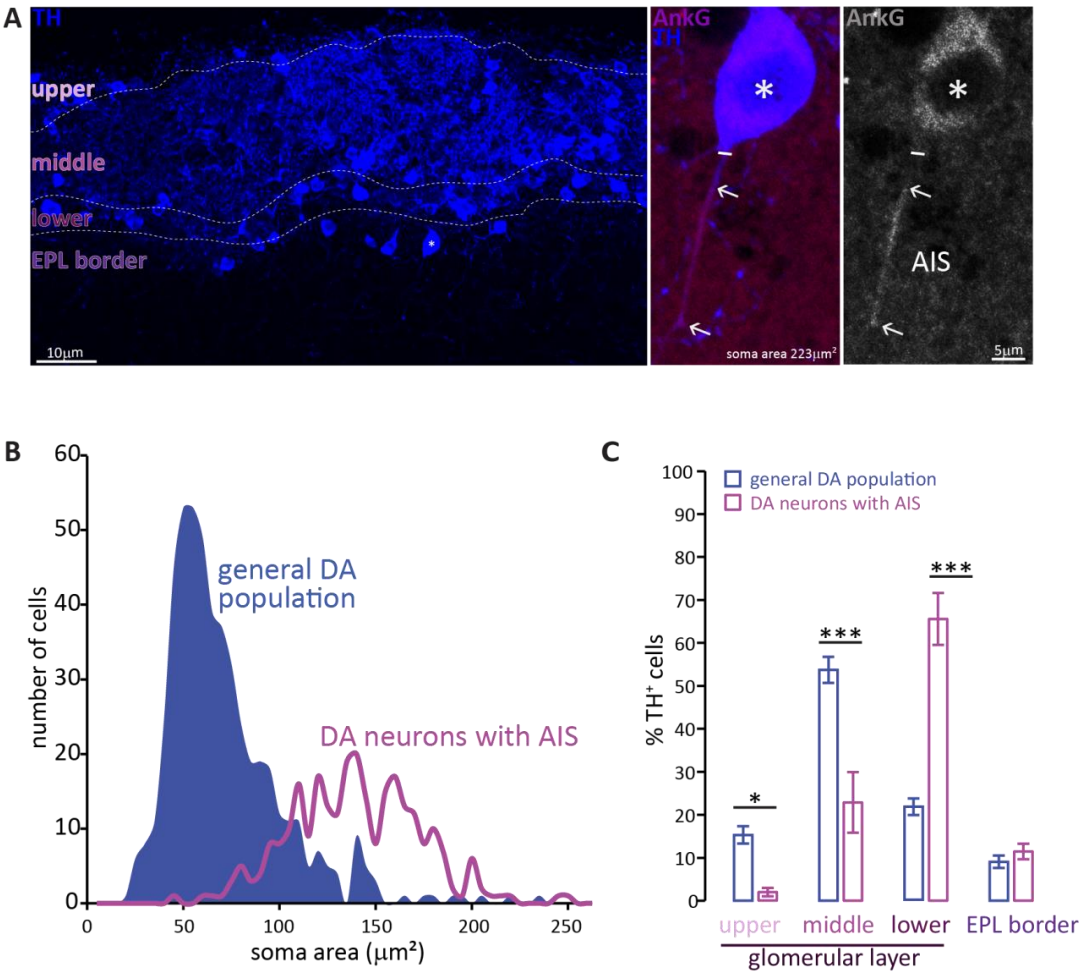

Figure 1. Two subtypes of DA neuron can be characterised based on size, location and presence of an AIS.

A. Left: example image of olfactory bulb stained with an anti-TH antibody (blue). Dashed lines indicate subregions of the glomerular layer (GL). The asterisk indicates an AIS-positive DA cell. Middle, right: zoomed image of the asterisked cell from the left panel, co-stained for TH (blue) and the AIS marker ankyrin-G (AnkG, magenta or greyscale). The solid line indicates the emergence of the axonal process from the soma; arrows indicate AIS start and end positions.

B. Frequency plots showing soma area of the general DA population (blue, filled area, n=519, N=3), and of the subset of DA neurons that possesses an AIS (magenta line, n=271, N=6).

C. Locations in the GL for both the general DA population (blue, mean±sem; n=888, N=6) and AIS-positive DA neurons (magenta, mean±sem; n=127, N=6). Post-hoc Sidak's test following 2-way repeated measures ANOVA; *, $p < 0.05$; ***, $p < 0.001$.

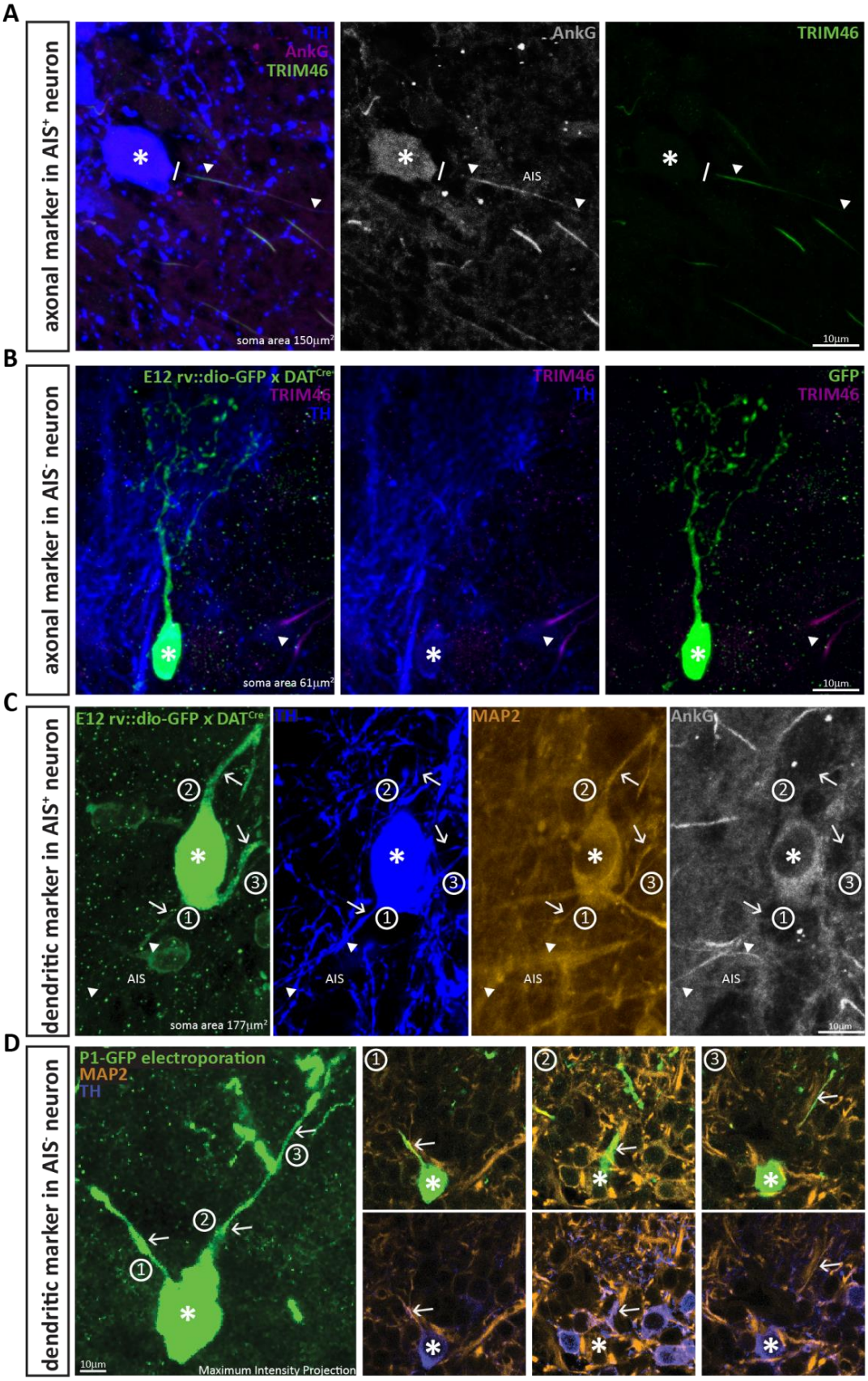

Figure 2. DA neurons that lack an AIS also lack the axonal marker TRIM-46, and all their processes co-stain with the dendritic marker MAP-2.

1210 **A.** Example image of a DA cell in a wild-type mouse stained for TH (blue), AnkG (magenta) and the
1211 axonal marker TRIM-46 (green). Asterisks indicate soma position; lines indicate the emergence of
1212 the axonal process from the soma; triangles indicate AIS start and end positions.

1213 **B.** Example image of an anaxonic DA cell in a DAT-Cre mouse injected at E12 with rv::dio-GFP, stained
1214 for TH (blue) and TRIM-46 (magenta). Asterisks indicate soma position; triangle shows a TRIM-46-
1215 and TH-positive process belonging to a neighbouring, non-GFP-expressing cell.

1216 **C.** Example image of an AIS-containing DA cell in a DAT-Cre mouse injected at E12 with rv::dio-GFP,
1217 stained for TH (blue), MAP-2 (orange) and AnkG (grey). Asterisks indicate soma position; triangles
1218 indicate AIS start and end positions; numbers and arrows indicate the three main processes
1219 emerging from the soma. Note that MAP-2 fluorescence in the axon (process 1) ends when AnkG
1220 fluorescence begins.

1221 **D.** Left: Maximum intensity projection image of an anaxonic DA cell in a wild-type mouse
1222 electroporated with GFP at P1, stained for TH (blue) and MAP-2 (orange). The asterisks indicates
1223 soma position; numbers and arrows indicate the three main processes emerging from the soma.
1224 Right: panels 1-3 show single z-plane images of each dendritic process, visualised with GFP plus
1225 MAP-2 label (top) or TH plus MAP-2 label (bottom). Note that all processes are positive for all three
1226 markers.

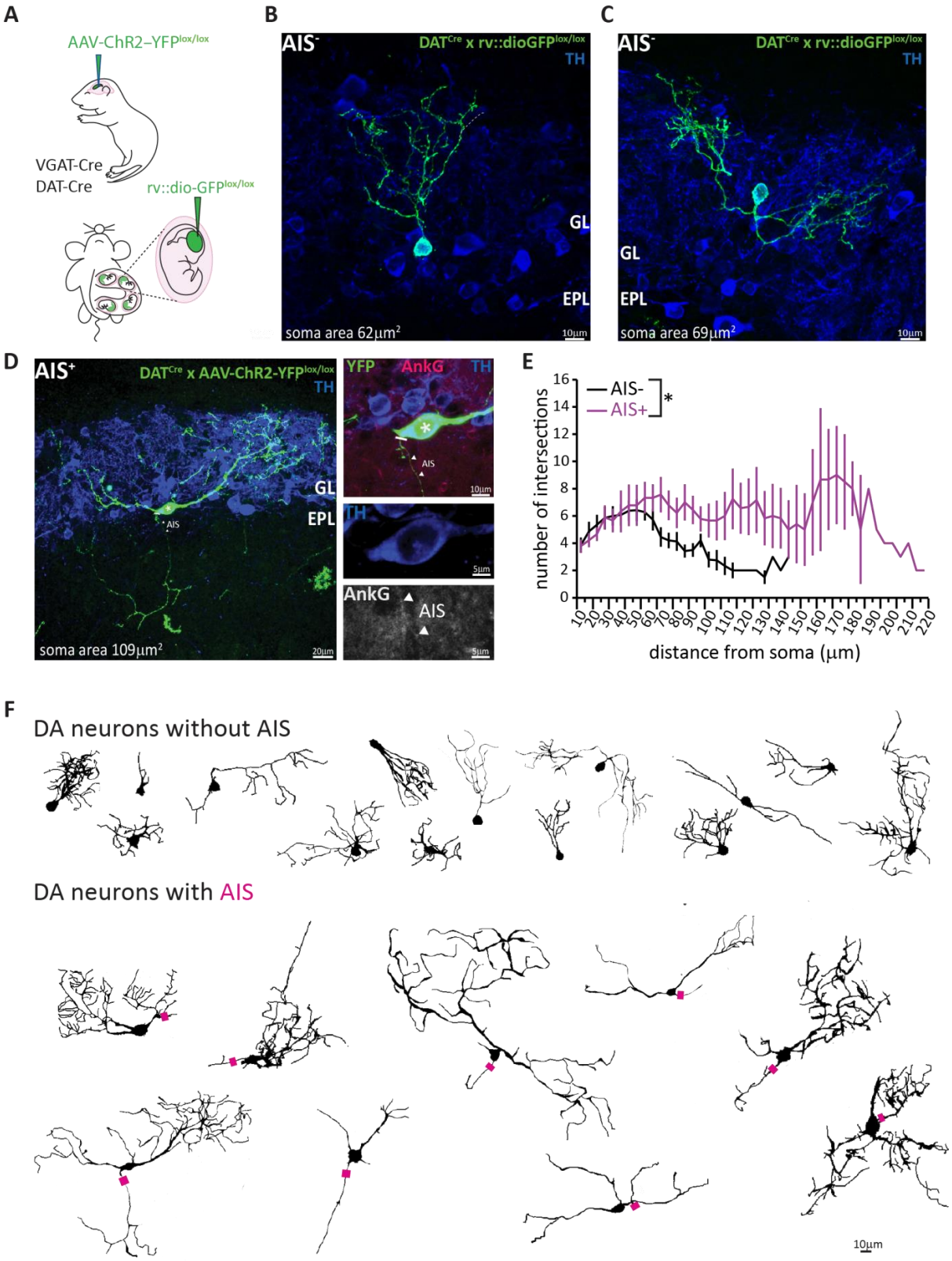

Figure 3. AIS-positive DA cells have more widely ramified dendritic morphology

A. Schematic representation of the experimental strategy adopted to achieve sparse labelling of DA cells: P1-2 neonates or E12 embryos from VGAT-Cre or DAT-Cre lines were injected with floxed AAV-YFP or rv:: dio-GFP viruses. Tissue was collected for analysis at P28.

B-C. Example images of OB DA cells sparsely labelled with GFP (green), co-stained for TH (blue). GL, glomerular layer; EPL, external plexiform layer. AIS-negative DA cells ramify their dendrites narrowly.

D. Example image of a GFP-labelled, AIS-positive DA cell which ramifies more broadly, co-stained for TH (blue) and AnkG (magenta). Right: zoomed insets showing GFP, TH and/or AnkG label; line indicates axon start; triangles show AIS start and end positions.

E. Sholl plots of branching patters for reconstructed DA neurons without (black, n=14) and with (magenta, n=9) an AIS. Data points are mean ± SEM ; effect of cell type in mixed model ANOVA; *, $p<0.05$; for further quantifications see Table 1.

F. Morphological reconstructions of 23 sufficiently sparsely-labelled DA neurons without (top) and with (bottom) an AIS. Approximate AIS location is indicated with a magenta square.

MORPHOLOGICAL PROPERTIES			
	AIS-negative (mean ± sem)	**AIS-positive** (mean ± sem)	**Test type, *p*-value**
Soma area (μm^2)	70.49 ± 2.71	139.00 ± 17.16	t^W**,** 0.003
Distance of soma from nerve layer (μm)	75.07 ± 12.79	141.60 ± 31.38	MW, 0.02
Number of primary dendrites	3.14 ± 0.23	3.44 ± 0.29	t, 0.43
Length of primary dendrites (μm)	12.14 ± 2.97	26.13 ± 5.23	MW, 0.01
Area under Sholl curve (μm)	338.60 ± 42.58	871.10 ± 167.20	t^W, 0.01
Furthest intersection (μm)	77.86 ± 8.23	148.30 ± 13.94	t, 0.0001
Maximum no. of intersections	8.36 ± 0.68	12.56 ± 1.68	t^W, 0.04
Radius for maximum no. of intersections (μm)	36.16 ± 4.45	80.00 ± 13.97	t^W**,** 0.02

Table 1. Morphological properties of AIS-negative and AIS-positive DA neurons.

Mean values ± SEM of morphological properties for sparsely labelled AIS-negative (n=14) and AIS-positive (n=9) DA cells. Statistical differences between groups (AIS-negative vs AIS-positive) were calculated with a Student's t test for normally-distributed data ("t"; with Welch correction "t^W") or with a Mann–Whitney test for non-normally distributed data ("MW"). Grey shading indicates significantly different measures. Morphological reconstructions and average Sholl plots are presented in Figure 3.

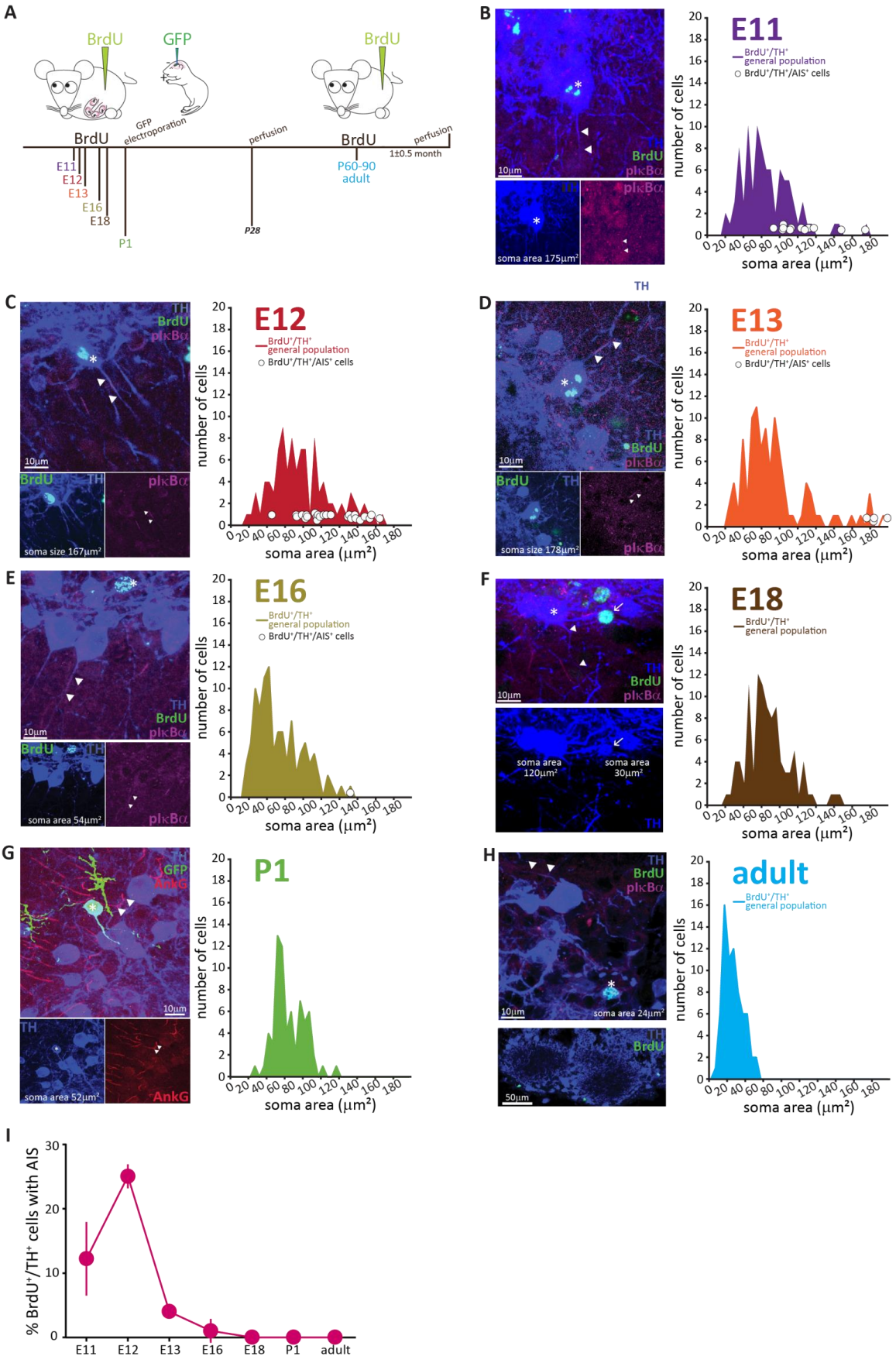

Figure 4. AIS-positive DA cells are generated exclusively in early embryonic development.

A. Schematic representation of the experimental strategy for birthdating experiments: pregnant wild-type mice were injected with a single dose of BrdU at different gestational days. Tissue was collected from their offspring at 1 month of age (P28), and also from the injected mothers which constitute the "adult" group. We also labelled neonatally-generated cells by electroporating GFP-encoding plasmid DNA injected into the lateral ventricles at P1.

B-H. Left: example images from OB slices stained with antibodies against BrdU (green), TH (blue) and the AIS markers pIκbα or AnkG (magenta). Asterisks indicate BrdU+/TH+ cells; triangles indicate AIS start and end positions; in E-H AISes are indicated in BrDU- cells for comparison. Right: soma area distribution of BrdU+/TH+ DA cells (for each BrdU time point n=100, N=3; for P1 electroporation n=68, N=3; for adult mothers n=70, N=2). Circles indicate AIS-positive cells (BrdU+/TH+/pIκbα+) at their respective soma size value.

I. Summary graph indicating the percentage of AIS-positive cells (BrdU+/TH+/pIκbα+) generated at each developmental time point (mean ± SEM). No AIS-positive DA cells were born after E18.

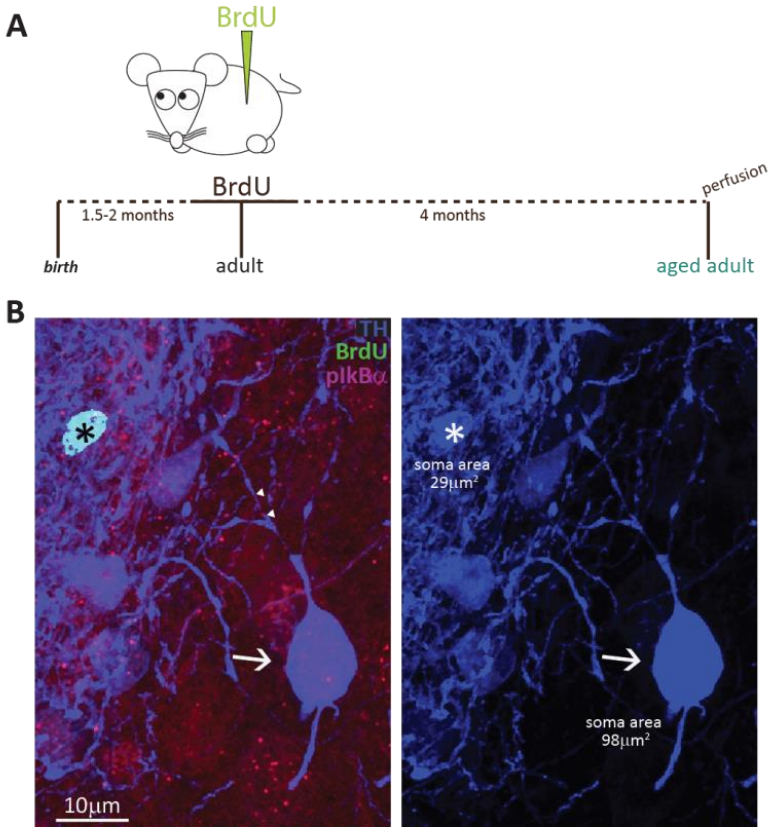

Figure 5. Fully mature adult-born DA neurons are small and never possess an AIS

A. Schematic representation of the experimental strategy: pregnant wild-type mice were injected with a single dose of BrdU, and their tissue was collected 4 months later to allow full maturation of adult-born neurons.

B. Example image of adult tissue perfused 4 months post BrdU injection, stained with antibodies against BrdU (green), TH (blue) and the AIS marker pIκbα (magenta). Asterisk indicates a BrdU+ DA

cell (TH+/ pIκbα-), triangles indicate AIS start and end positions; the arrow indicates a neighbouring large AIS+ DA neuron that is BrdU-negative.

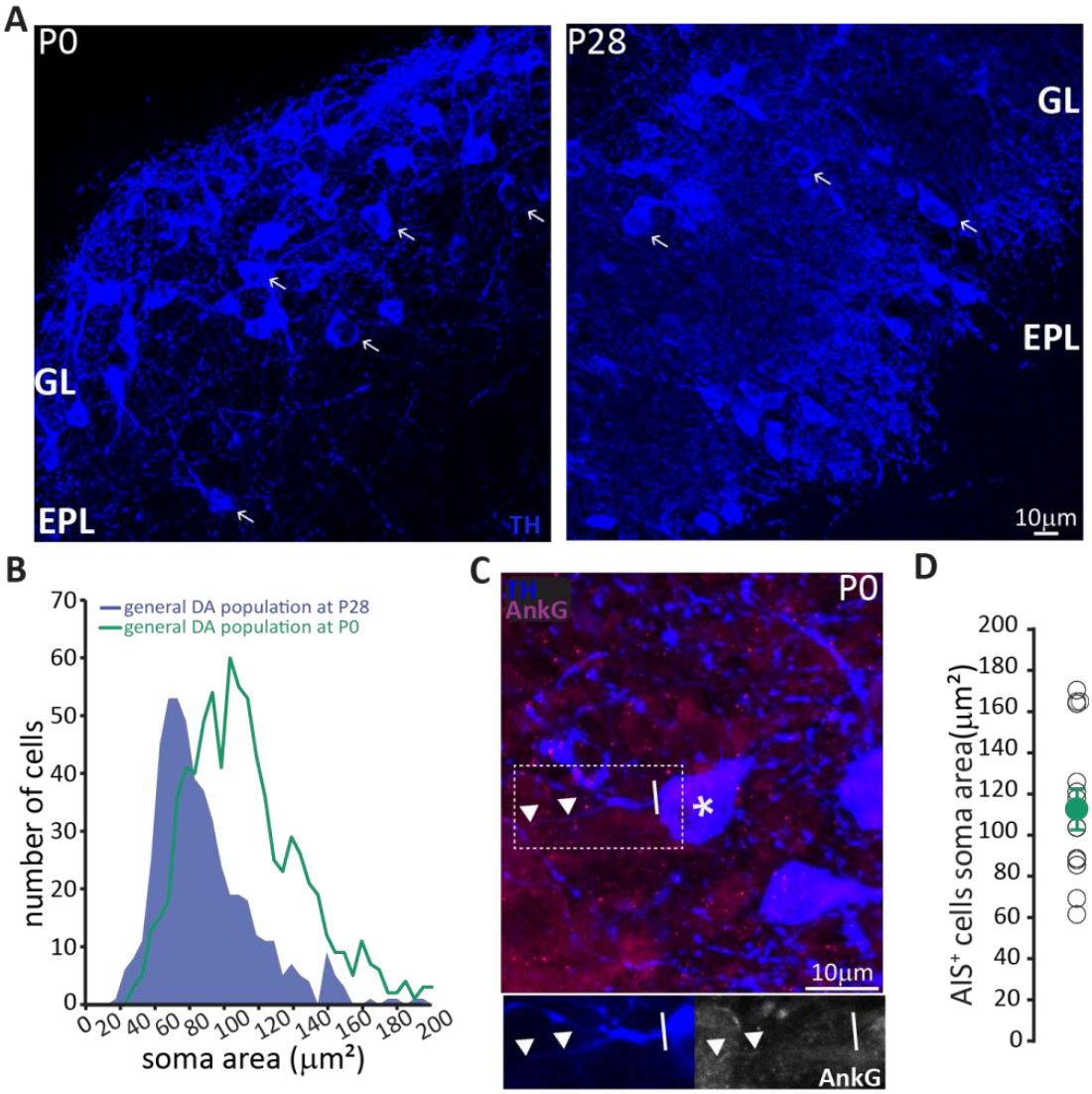

Figure 6. In neonates there is a preponderance of large DA neurons that can already possess an AIS.

A. Low magnification example images of tissue from P0 and P28 wild-type mice stained with an antibody against TH (blue). Arrows indicate cells with a soma area bigger than 100 mm2; "GL" indicates glomerular layer, "EPL" indicates external plexiform layer.

B. Soma area distribution of TH+ DA cells in P0 mice (teal, n=781, N=3), overlaid on the soma area distribution of the general DA cell population at P28 (blue filled line; see Fig. 1B); Kolmogorov-Smirnov test between the two distributions **, D= 0.3581, p<0.01.

C. High magnification example image of tissue from a P0 mouse stained with antibodies against TH (blue) and AnkG (magenta). Asterisk indicates the soma of an AIS-positive cell; dashed lines show the inset area magnified below; solid line shows axon start; triangles indicate AIS start and end

positions.

D. Soma area of TH+/AnkG+ DA cells in P0 mice. Empty circles represent individual cells, full circle shows mean ± SEM (110 ± 10 mm2; n=16, N=2).

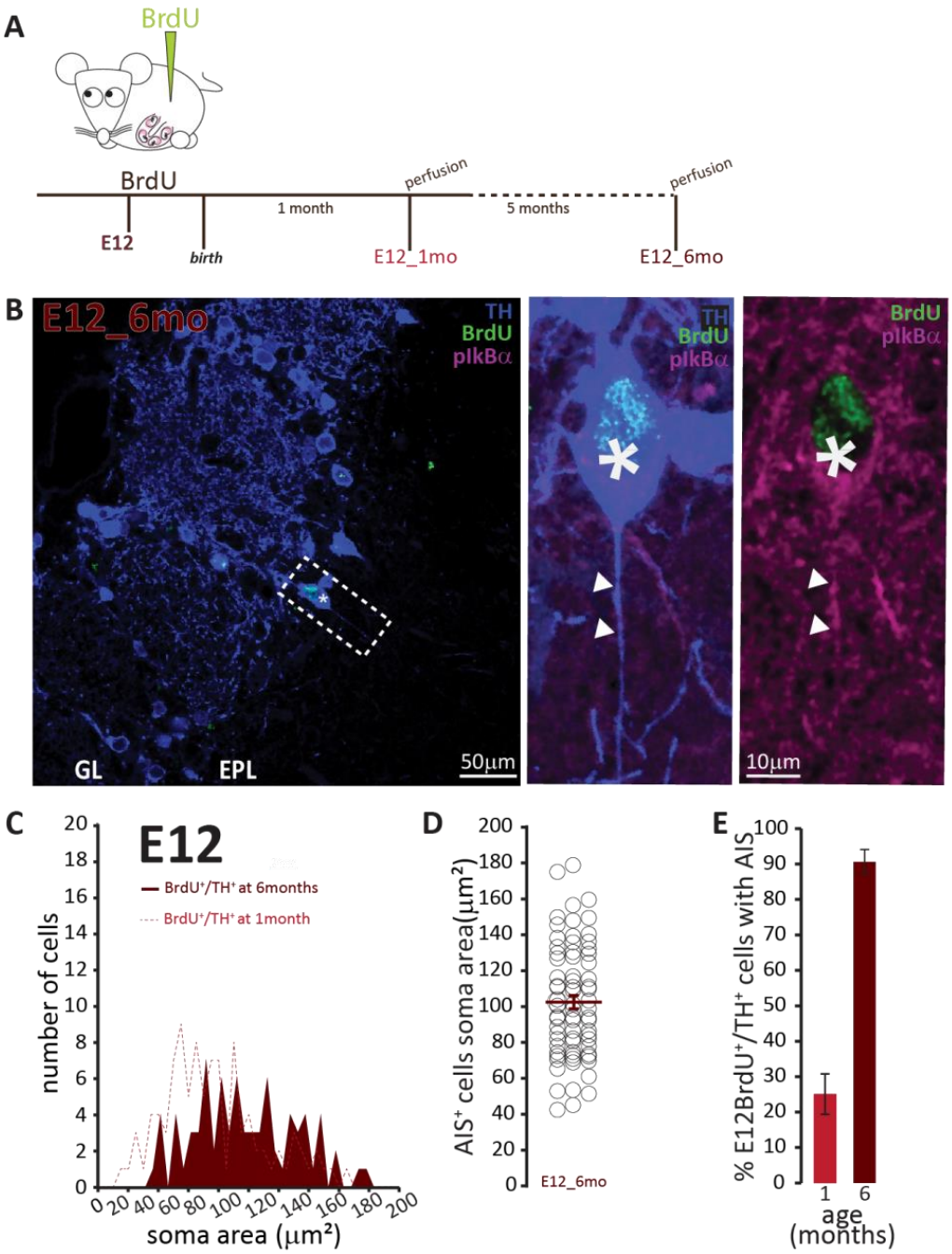

Figure 7. AIS-positive cells form the vast majority of embryonically-generated DA neurons that persist throughout adult life.

A. Schematic representation of the experimental strategy: pregnant wild-type mice were injected with a single dose of BrdU at E12. Tissue was collected from their offspring when they reached 6 months of age and compared with data collected from littermates perfused at 1 month of age (data

1298 shown in Fig 6C).

1299 **B.** Left: Low magnification example image of 6-month-old tissue stained with antibodies against BrdU
1300 (green), TH (blue) and the AIS marker pIκBα (magenta). GL, glomerular layer; EPL, external plexiform
1301 layer; asterisk indicates an E12-6mo BrdU+/TH+ DA cell; dashed line indicates the inset magnified on
1302 the right. Right: magnified example image of an E12-6mo BrdU+/TH+/pIκBα+ cell; solid line indicates
1303 axon start; arrows show AIS start and end positions.

1304 **C.** Soma area distribution of E12-6mo BrdU+/TH+ DA cells (dark red, n=78, N=4), overlaid on the
1305 soma area distribution of E12-1mo BrdU+/TH+ DA cells (dashed light red line; see Fig. 4C).

1306 **D.** Soma area of E12-6mo BrdU+/TH+/pIκBα+ DA cells. Empty circles represent individual AIS-
1307 positive neurons, dark red lines show mean ± SEM (102 ± 4 mm2; n=71, N=4).

1308 **E.** Mean ± SEM percentage of AIS-positive E12-BrdU+/TH+ DA cells in tissue from 1-month-old (light
1309 red, 25%; n=100, N=3) and 6-month-old (dark red, 91%; n=78, N=4) mice.

1310

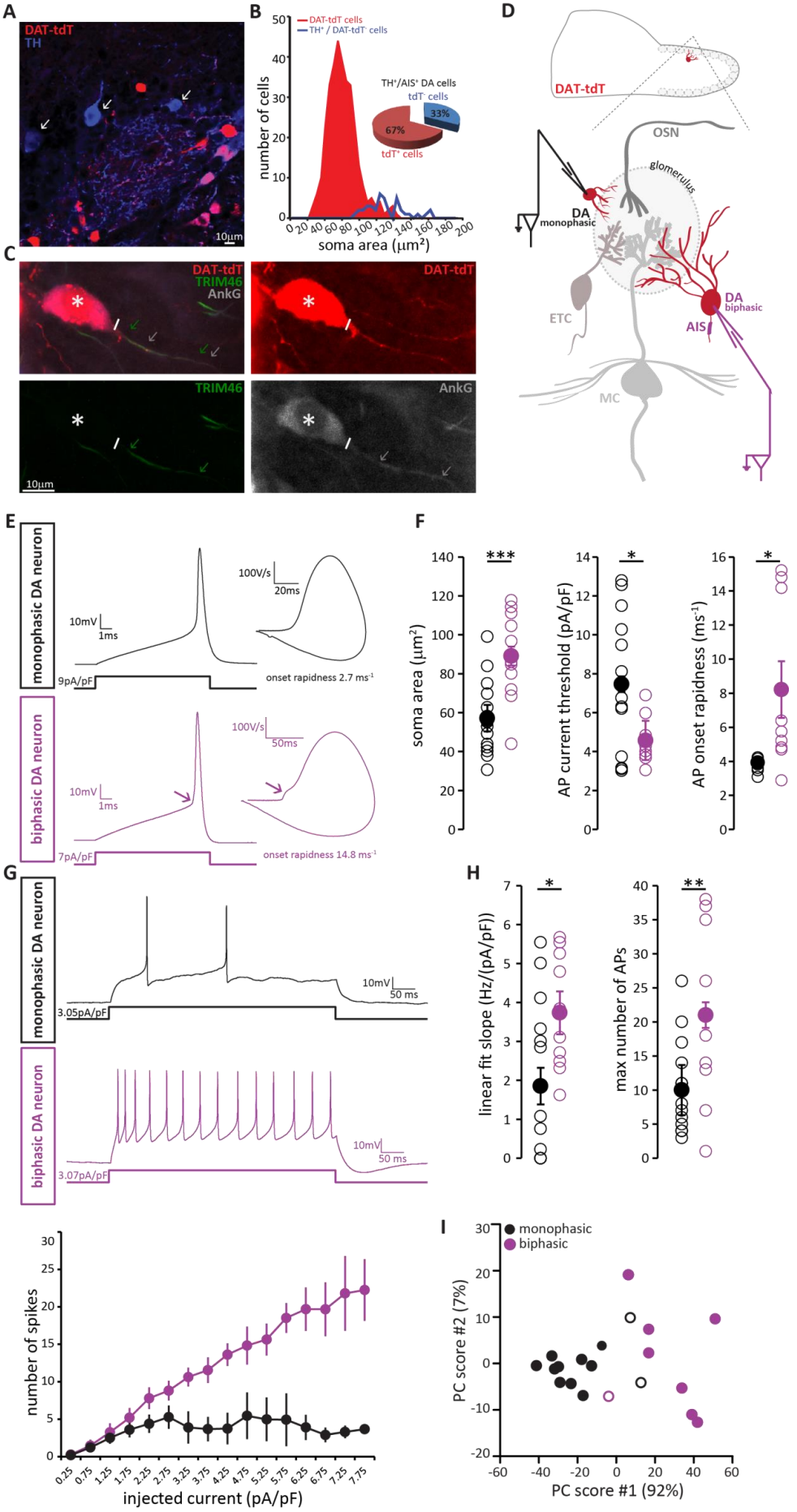
A
DAT-tdT
TH
10µm
B
DAT-tdT cells
TH+ / DAT-tdT- cells
number of cells
soma area (µm²)
TH+/AIS+ DA cells
tdT- cells
33%
67%
tdT+ cells
C
DAT-tdT
TRIM46
AnkG
10µm
D
DAT-tdT
OSN
glomerulus
DA
monophasic
ETC
DA
biphasic
AIS
MC
E
monophasic DA neuron
10mV
1ms
9pA/pF
100V/s
20ms
onset rapidness 2.7 ms-1
biphasic DA neuron
10mV
1ms
7pA/pF
100V/s
50ms
onset rapidness 14.8 ms-1
F
soma area (µm²)
AP current threshold (pA/pF)
AP onset rapidness (ms-1)
G
monophasic DA neuron
3.05pA/pF
10mV
50 ms
biphasic DA neuron
3.07pA/pF
10mV
50 ms
H
linear fit slope (Hz/(pA/pF))
max number of APs
number of spikes
injected current (pA/pF)
I
monophasic
biphasic
PC score #2 (7%)
PC score #1 (92%)

1311

1312 **Figure 8.** AIS-positive DA neurons have greater intrinsic excitability

1313 **A.** Example image of a fixed, 50 µm OB slice from a P28 DAT-tdT (red) mouse, immunostained with
1314 an anti-TH antibody (blue). While most TH-positive neurons exhibit red tdT fluorescence, some are
1315 tdT-negative (arrows).

1316 **B.** Soma size distributions of all DAT-tdT-positive cells (red), and of DA neurons that are DAT-tdT-
1317 negative but TH-positive (blue). Inset: percentages of AIS-positive/TH-positive DA cells that are either
1318 tdT-positive or –negative (n=50, N=5).

1319 **C.** Example image of a DAT-tdT-labelled DA cell (red) stained with the axonal marker TRIM-46 (green)
1320 and the AIS marker AnkG (greyscale). Asterisks indicate the soma; line indicates axon start; arrows
1321 indicate start and end position of the TRIM (green) and AnkG (white) label.

1322 **D.** Schematic representation of the experimental strategy for whole-cell recordings: acute

1323 300 µm OB slices were obtained from P21-35 DAT-tdT mice, and tdT-positive DA cells of either
1324 subtype were targeted for whole-cell patch-clamp recording.

1325 **E.** Example current-clamp traces of single APs fired by monophasic (AIS-negative, black, n=15) and
1326 biphasic (AIS-positive, magenta, n=11) DAT-tdTomato neurons. Left: action potentials fired to
1327 threshold 10 ms somatic current injection. Right: phase plane plots of the spikes shown on the left.
1328 Arrow points to the AIS-dependent first action potential phase.

1329 **F.** Quantification of soma area (t-test; ***, p = 0.0006), current threshold (Welch-corrected t-test; *,
1330 p = 0.017), and onset rapidness (Welch-corrected t-test; *, p = 0.035) in monophasic and biphasic
1331 cells. Empty circles show values from individual cells, filled circles show mean ± SEM.

1332 **G.** Top: Example current-clamp traces of multiple APs fired in response to a 300pA / 500 ms somatic
1333 current injection in monophasic and biphasic cells. Bottom: input-output curve of injected current
1334 density versus mean ±SEM spike number for each group.

1335 **H.** Quantification of input-output slope (t-test; *, p=0.044), and of the maximum number of action
1336 potentials fired by each cell over the whole range of injected current intensities (t-test; **, p =
1337 0.0092). Empty circles show values from individual cells; filled circles show mean ± SEM.

1338 **I.** Classification of DAT-tdT neurons based on values obtained from whole-cell recordings. Each circle
1339 shows one cell, plotted according to its primary and secondary PCA component scores (these
1340 components accounted for 92% and 7% of the variance in the data, respectively). Filled circles show
1341 cells correctly classified by k-means analysis; open circles show the few cells (3/26 overall) that were
1342 incorrectly classified.

1343

1344

1345

1346

INTRINSIC ELECTROPHYSIOLOGICAL PROPERTIES			
	Monophasic (mean ± sem)	**Biphasic** (mean ± sem)	**Test type, *p*-value**
PASSIVE PROPERTIES			
Soma area (μm^2)	57 ± 4.8	89 ± 6.8	**t, <0.01**
Membrane capacitance (pF)	19 ± 2	22 ± 2	t, 0.39
Resting membrane potential (mV)	-78 ± 1.9	-74 ± 2.9	MW, 0.31
Input Resistance (MΩ)	725 ± 136	572 ± 115	MW, 0.32
ACTION POTENTIAL PROPERTIES			
Threshold (pA/pF)	7.5 ± 1.0	4.6 ± 0.4	**t, 0.02**
Threshold (mV)	-30 ± 1.0	-33 ± 1.0	t, 0.13
Max voltage reached (mV)	19 ± 2.4	18 ± 4.0	t, 0.80
Peak amplitude (mV)	49 ± 2.2	50 ± 4.4	t, 0.79
Width at half-height (ms)	0.55 ± 0.03	0.50 ± 0.04	t, 0.37
Rate of rise (max dV/dt) (mV/ms)	230 ± 16	251 ± 31	t, 0.53
Onset rapidness (1/ms)	3.95 ± 0.28	8.22 ± 1.66	**t, 0.03**
After hyper polarization AHP (mV)	-54 ± 1.4	-55 ± 1.5	t, 0.72
AHP relative to threshold (mV)	25 ± 1.3	24 ± 1.3	t, 0.95
REPETITIVE FIRING PROPERTIES			
Rheobase (pA/pF)	3.6 ± 1.0	1.7 ± 0.8	MW, 0.28
Max number of action potentials	10 ± 2	21 ± 4	**t, 0.01**
First action potential delay (ms)	168 ± 38	273 ± 45	t, 0.08
Inter-spike interval CV	0.28 ± 0.04	0.24 ± 0.32	t, 0.46
Slope of input/output curve (Hz/(pA/pF))	1.85 ± 0.54	3.53 ± 0.48	**t, 0.04**

Table 2. Intrinsic electrophysiological properties of DAT-tdTomato neurons.

Mean values ± SEM of passive, action potential and repetitive firing properties for monophasic (putative AIS-negative, n=15) and biphasic (putative AIS-positive, n=11) DAT-tdTomato cells. Statistical differences between groups (monophasic vs biphasic) were calculated with a Student's t test for normally-distributed data ("t") or with a Mann–Whitney test for non-normally distributed data ("MW"). Grey shading indicates statistically different measures, for which individual data points and example traces are presented in Figure 8.

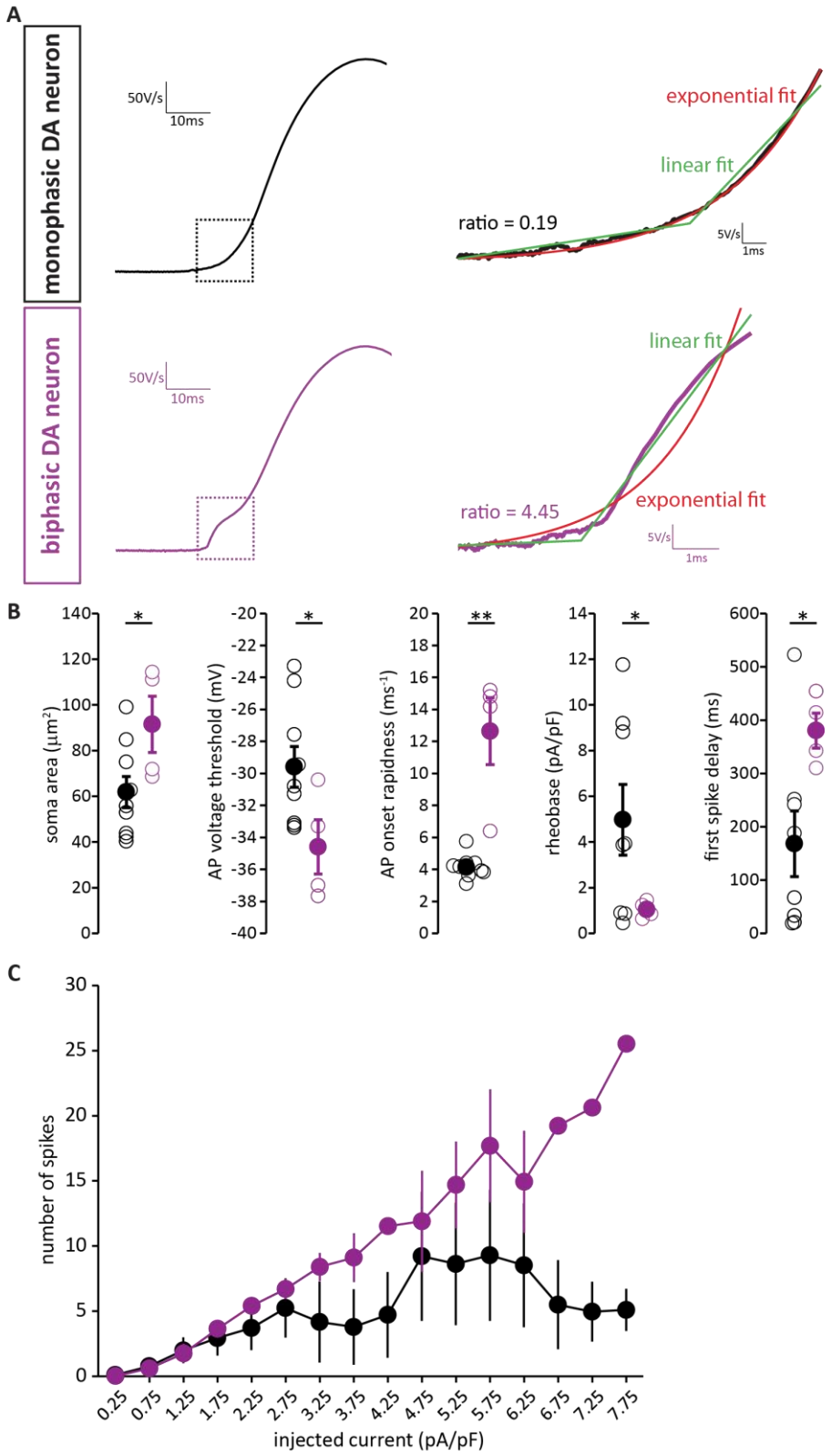

Figure 8 – figure supplement 1. AIS-positive DA neurons also have greater intrinsic excitability with strict, objective phase plane plot classification.

A. Example current-clamp traces of phase plane plots of single APs fired by monophasic (AIS-negative, black, top) and biphasic (AIS-positive, magenta, bottom) DAT-tdTomato neurons. Dashed box indicates the AIS-dependent first action potential phase, which is shown at higher detail on the

right and fitted with two methods. The ratio between the errors of the linear fit (green) and the exponential fit (red) is indicated near the trace.

B. Quantification of soma area (t-test; p = 0.04), voltage threshold (t-test; p = 0.046), onset rapidness (Mann-Withney test; p = 0.003), rheobase (t-test; p = 0.039) and first spike delay (t-test; p = 0.0431) in monophasic and biphasic cells. Empty circles show values from individual cells, filled circles show mean ± SEM; *, p < 0.05; **, p < 0.01.

C. Input-output curve of injected current density versus mean ±SEM spike number for each group.

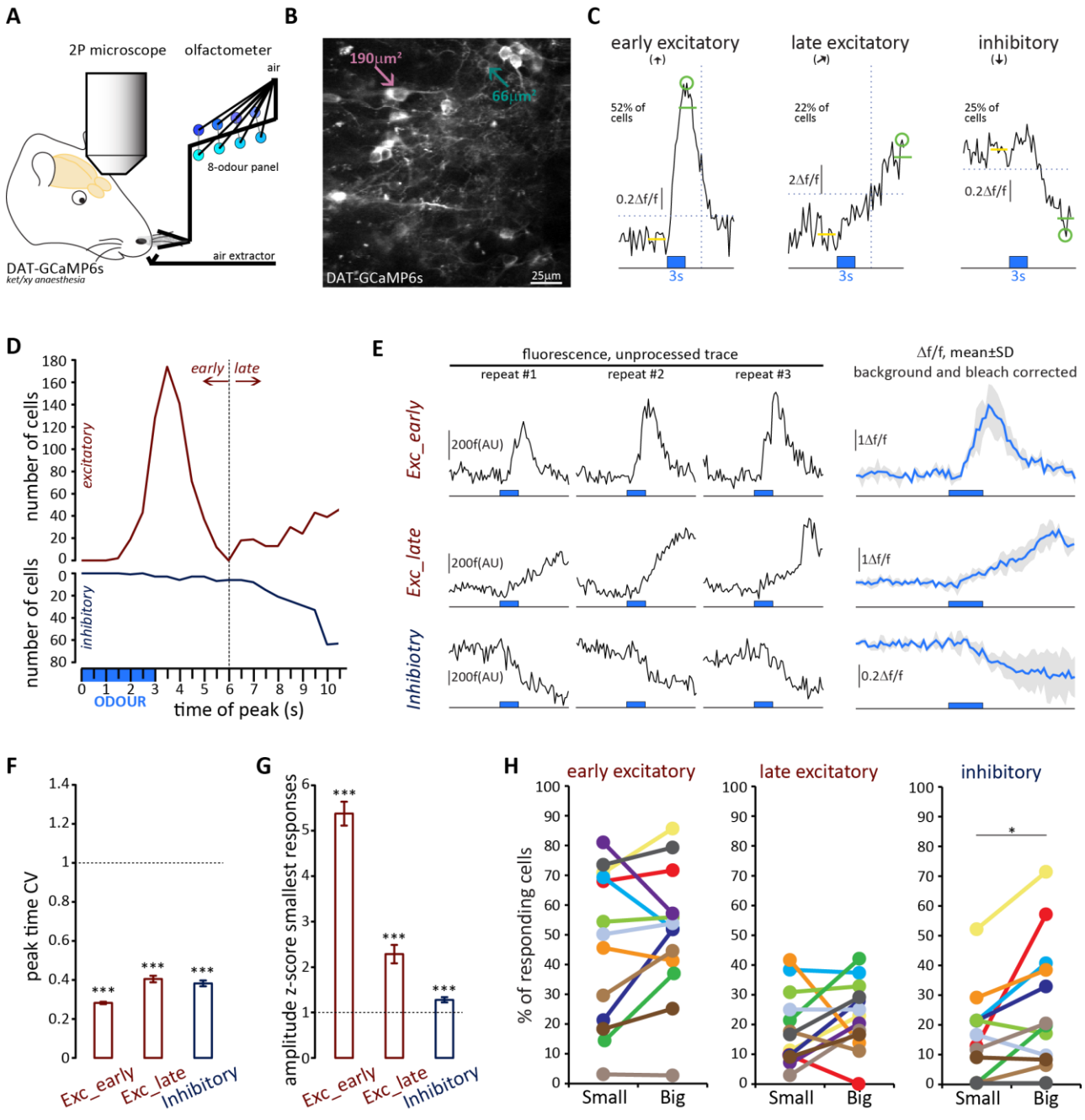

Figure 9. Both OB DA cell subtypes display diverse odour response types.

A. Schematic representation of the experimental strategy for in vivo recordings: adult DAT-GCaMP6s mice (anaesthetised with ketamine/xylazine) were presented with a panel of eight odours. Resulting changes in GCaMP fluorescence in DA neurons were imaged through a cranial window positioned over the OB.

B. Example field of view of the deeper part of the glomerular layer used for image acquisition (sum intensity projection of time axis, enhanced contrast). Fields of view were selected so as to contain both 'big' (soma area > 99 mm2, putatively AIS-positive; magenta arrow) and 'small' (soma area < 70 mm2, putatively AIS-negative; green arrow) DA neuron types.

C. Representative examples of the three categories of Df/f GCaMP responses that we observed in the dataset. Deflections from baseline were considered events when they exceeded a threshold (horizontal dashed line) set at 3 times the baseline standard deviation. Excitatory responses occurred either quickly after odour presentation (early excitatory responses,[h]; recorded in 52% of cells) or on a later timeframe (late excitatory responses, [k]; recorded in 22% of cells). The early/late cut-off value was 6 s (vertical dashed line; see Methods). Approximately a fifth of all cells also showed supra threshold negative deflection from baseline (inhibitory responses [i]; present in 25% of cells). Green circle indicates absolute maximum or minimum value (peak) and green line shows the mean of the 3s around the peak; yellow line indicates the 3 sec of baseline prior to odour presentation (blue box).

D. Time of peak frequency plot for excitatory (red) and inhibitory (blue) events occurring after 3s odour presentation (blue bar). The vertical dashed line indicates the cut-off value for early (≤ 6 s) and late (> 6 s) excitatory responses.

E. Left: Raw fluorescence traces of early-excitatory, late-excitatory and inhibitory responses to 3 repeated presentations of a 3 s odour stimulus (blue box). Right: Mean Δf/f response over the three repeats, after background subtraction and bleach correction. Grey shading indicates standard deviation (SD).

F. Mean ± SEM coefficient of variation (CV) of peak time over the three odour presentations for early excitatory, late excitatory and inhibitory responses. Wilcoxon test vs. 1; ***, $p < 0.001$.

G. Mean ± SEM amplitude z-score value (mean of the two smallest responses out of the three odour repeats) for early excitatory, late excitatory and inhibitory responses. Wilcoxon test vs. 1; ***, $p < 0.001$.

H. Percentage of small (putative AIS-negative) and big (putative AIS-positive) cells in each mouse that showed at least one early excitatory (left), late excitatory (middle) or inhibitory (right) response. Colour-coding indicates the 13 mice that were imaged. Wilcoxon paired rank test; *, $p < 0.05$.

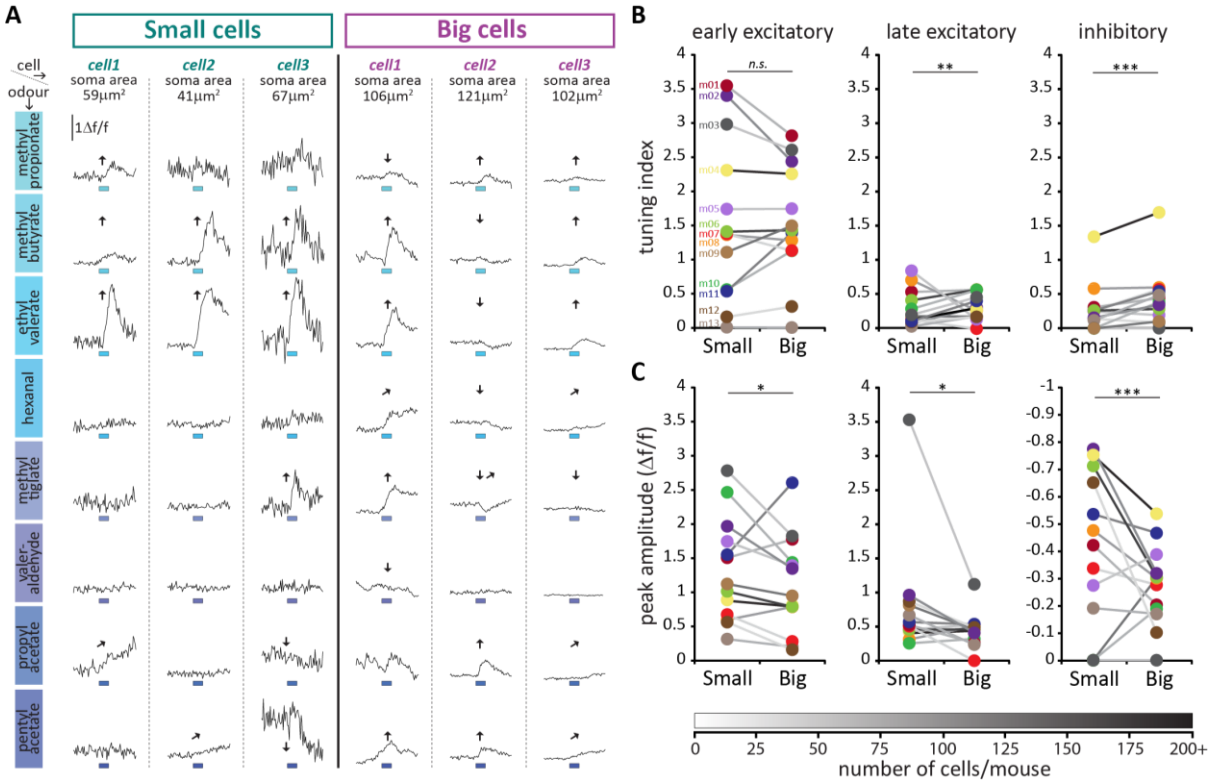

Figure 10. Large putative AIS-positive DA cells respond less strongly to odours and are more broadly tuned.

A. Example Δf/f GCaMP responses to the eight odours (rows, 3s stimulus timing is indicated by blue shaded bars) for three big and three small example cells (columns; soma areas are indicated below the responses) imaged in the same mouse. Significant responses are indicated as: h early excitatory, k late excitatory, i inhibitory.

B. Mean values of odour tuning indices for early excitatory (left), late excitatory (middle) and inhibitory responses (right) measured in small and big cells. Coloured dots indicate mean values for each cell type from each of the 13 imaged mice. The grayscale colour of the connecting lines indicates the number of recorded cells for each mouse (scale below). Cell-type effect in multilevel ANOVA; n.s., non-significant; *, $p < 0.05$; **, $p < 0.01$.

C. Similar to B. Median values of odour peak intensity for early excitatory (left), late excitatory (middle) and inhibitory responses (right). Cell-type effect in multilevel ANOVA; *, $p < 0.05$; ***, $p < 0.0001$.

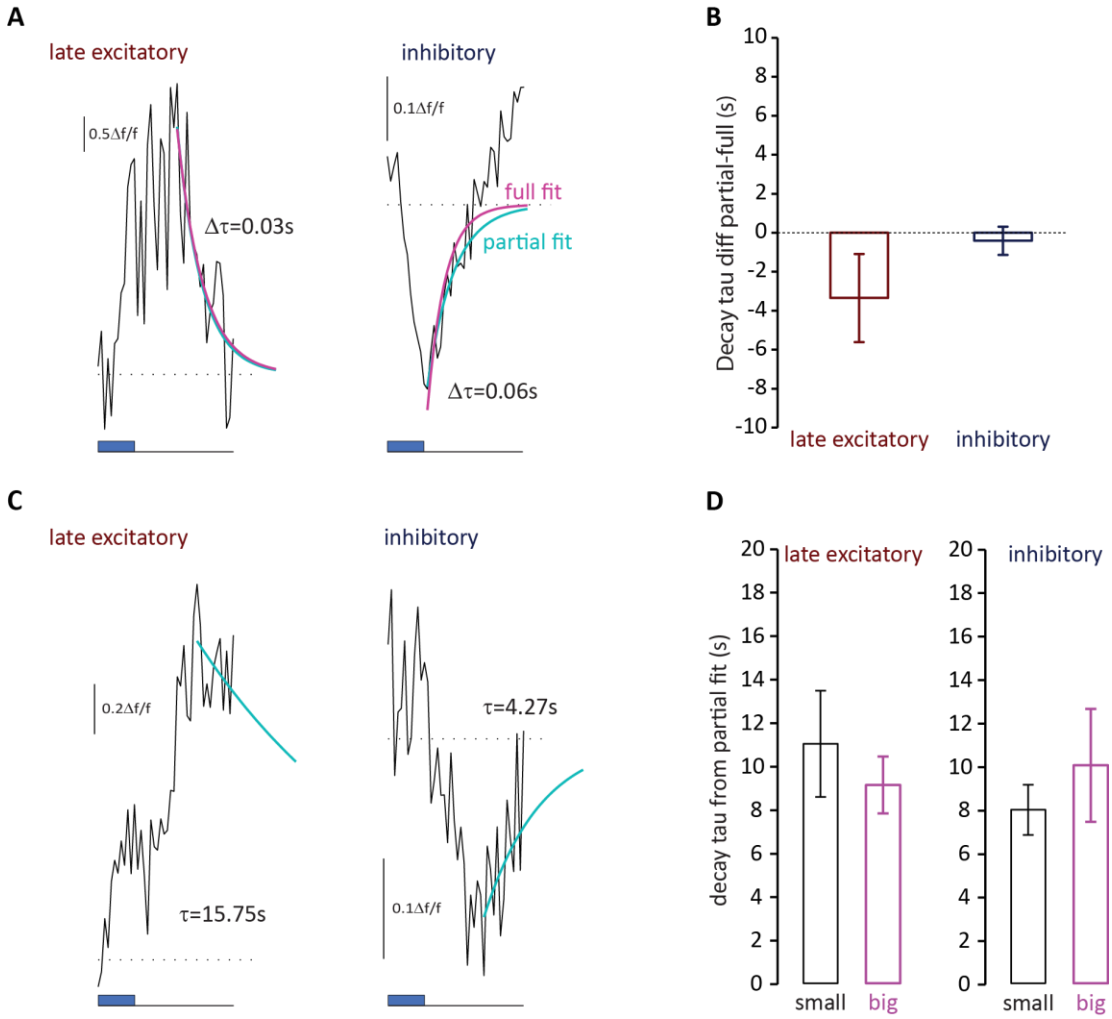

Figure 10 – figure supplement 1. Decay kinetics of late-latency responses do not differ between small and big OB DA neurons.

A. Example mean traces of late-latency excitatory and inhibitory responses that returned to baseline within the imaging timeframe (10.5 s after stimulus onset). Blue box shows stimulus timing; dotted line shows baseline Δf/f; blue line indicates exponential fit to the first 10 points from the peak only (partial); magenta line indicates exponential fit plotted to the whole trace from the peak (full). Values for the difference between the two decay constants from the fits displayed for each trace.

B. Mean ± SEM differences between decay constants from whole-trace fit (full) and first-10-points fit (partial) for each response type (late excitatory n = 14; inhibitory n = 44; Wilcoxon test vs. 0, late excitatory p = 0.50; inhibitory p = 0.17).

C. Example mean traces of late-latency excitatory and inhibitory responses whose decay could be estimated with an exponential fit to the first ten points following the response peak (blue line). Decay constants are shown for each trace.

D. Mean ± SEM partial fit decay constants for small and big cell late excitatory and inhibitory response types (late excitatory, fixed effect of cell type in multilevel ANOVA, $F_{1,98} = 0.32$, $p = 0.57$; inhibitory, $F_{1,113} = 0.078$, $p = 0.78$).